

**SIMULATION AND FABRICATION OF
THIN FILM NOTCH FILTER**



M.Sc. THESIS

Eray HUMALI

Department of Materials and Metallurgical Engineering

Materials Engineering Programme

JULY 2020

**SIMULATION AND FABRICATION OF
THIN FILM NOTCH FILTER**

M.Sc. THESIS

**Eray HUMALI
(506171431)**

Department of Materials and Metallurgical Engineering

Materials Engineering Programme

Thesis Advisor: Prof. Dr. M. Kürşat KAZMANLI

JULY 2020

**İNCE FİLM OPTİK EKSİLTME FİLTRE
BENZETİMİ VE ÜRETİMİ**

YÜKSEK LİSANS TEZİ

**Eray HUMALI
(506171431)**

Metalurji Malzeme Mühendisliği Bölümü

Malzeme Mühendisliği Programı

Tez Danışmanı: Prof. Dr. M. Kürşat KAZMANLI

TEMMUZ 2020

Eray HUMALI, a M.Sc. student of ITU Graduate School of Science Engineering and Technology 506171431 successfully defended the thesis entitled “SIMULATION AND FABRICATION OF THIN FILM NOTCH FILTER”, which he/she prepared after fulfilling the requirements specified in the associated legislations, before the jury whose signatures are below.

Thesis Advisor : **Prof. Dr. M. Kürşat KAZMANLI**
Istanbul Technical University

Jury Members : **Assist. Prof. Dr. Nuri SOLAK**
Istanbul Technical University

Assist. Prof. Dr. Garip ERDOĞAN
Sakarya University

.....

.....

.....

Date of Submission : **16.06.2020**

Date of Defense : **14.07.2020**





to my mom and dad...



FOREWORD

It would not have been to complete this study without help and support of people around me. I would like to give particular mention here for some of them.

I would like to express my sincere gratitude to my advisor Prof. Dr. M. Kürşat KAZMANLI for the help of my research with his immense knowledge, motivation, and great patience.

I would like to thank to my colleagues İ. Göksel HIZLI and Süleyman ÇELİK for their help during experimental procedures.

I also would like to thank my colleagues and best friends B. Başak YILMAZ, Canay DEMİR, and Umur C. KAYA for their continuous personal motivation and support.

Finally, I would like to thank to my family for their love, trust, and support throughout my life.

July 2020

Eray HUMALI

TABLE OF CONTENTS

	<u>Page</u>
FOREWORD.....	ix
TABLE OF CONTENTS.....	xi
ABBREVIATIONS	xiii
SYMBOLS.....	xv
LIST OF TABLES	xvii
LIST OF FIGURES	xix
SUMMARY	xxi
ÖZET	xxiii
1. INTRODUCTION	1
1.1 Historical Background of Light: Wave-Particle Duality	1
1.2 Optical Filters	2
1.2.1 Absorptive filters	2
1.2.2 Interference filters.....	3
1.3 The Content of Study.....	5
2. OPTICAL BEHAVIOR OF THIN FILMS: PHYSICAL PRINCIPLES	7
2.1 Thin Film	7
2.2 Optical Basics	8
2.3 Parameters of Refractive Index.....	14
2.3.1 Wavelength	14
2.3.2 Mass density	16
2.3.3 Temperature	16
2.3.4 Impurity	16
3. NUMERICAL MODELING OF THIN FILM NOTCH FILTER	17
3.1 Material Selection.....	17
3.2 Single-layer Modeling.....	19
3.3 Multilayer Modeling.....	19
4. THIN FILM FABRICATION TECHNIQUES	21
4.1 Chemical Vapor Deposition.....	21
4.2 Physical Vapor Deposition	23
4.2.1 Sputtering	23
4.2.1.1 Diode.....	24
4.2.1.2 Magnetron.....	25
4.2.2 Evaporative	26
4.2.2.1 Resistive.....	27
4.2.2.2 Electron Beam	27
5. EXPERIMENTAL PROCEDURES.....	31
5.1 Thin Film Coating System.....	31

5.1.1 The vacuum chamber.....	31
5.1.2 The vacuum control unit.....	32
5.1.3 The E-beam control unit.....	32
5.1.4 Thickness monitoring system.....	32
5.2 Selection of Coating Materials	33
5.2.1 Al ₂ O ₃	33
5.2.2 Y ₂ O ₃	34
5.2.3 SiO ₂	34
5.3 Experiments, Analysis, and Results	35
5.3.1 Surface analysis	35
5.3.2 Thickness measurement.....	37
5.3.3 Optical Behaviors	39
5.3.3.1 Single-layer.....	39
5.3.3.2 Multilayer	44
5.4 Discussions	51
6. CONCLUSION	55
REFERENCES.....	59
APPENDICES.....	63
APPENDIX A.1	65
APPENDIX A.2	66
APPENDIX A.3	67
CURRICULUM VITAE.....	70

ABBREVIATIONS

PVD	: Physical Vapor Deposition
CVD	: Chemical Vapor Deposition
FWHM	: Full-width at half maximum
E-beam	: Electron beam
CIP	: Cold isostatic pressing
AFM	: Atomic force microscopy





SYMBOLS

n_i	: Refractive index
t_i	: Thickness of thin film
λ	: Wavelength
π	: Number of pi
k	: Wave number
Δ	: Optical path difference
δ	: Phase difference
\vec{E}	: Electric field vector
\vec{B}	: Magnetic field vector
μ_0	: Permeability of space
ϵ_0	: Permittivity of space
ρ	: Density
v	: Speed of light in medium
c	: Speed of light in space
T	: Transmittance
R	: Reflectance
A	: Absorptance
M_i	: Thin film characteristic matrix
N	: Number of periodic thin film groups
S	: Sputtering yield
β	: Dimensionless simulation constant
c_λ	: Center wavelength of notch filter



LIST OF TABLES

	<u>Page</u>
Table 3.1 : Chosen materials and their Sellmeier dispersion equations.	18
Table 5.1 : The general features of Al_2O_3 [29].	34
Table 5.2 : The general features of Y_2O_3 [30].	34
Table 5.3 : The general features of SiO_2 [31].	35
Table 5.4 : Surface roughness of single-layer coatings.	36
Table 5.5 : Measured film thickness comparison by the thickness monitoring system and surface profiler.	38
Table 5.6 : Adjusted mass density of the coating materials.	39
Table 5.7 : Comparison of expected and measured film thickness.	44
Table 5.8 : Absolute thickness deviation ratio of simulation and measurement. ...	44
Table 5.9 : Specifications of the produced thin film notch filters.	54



LIST OF FIGURES

	<u>Page</u>
Figure 1.1 : Electromagnetic spectrum [8].	4
Figure 2.1 : The path of incident electromagnetic wave on surfaces.	7
Figure 2.2 : Transmission and reflection from the single-layer thin film [13].	9
Figure 3.1 : Wavelength-dependent refractive index of chosen materials	18
Figure 3.2 : Multilayer stack.	20
Figure 4.1 : Basic cold-wall CVD system and deposition mechanism [13].	22
Figure 4.2 : Schema of the diode sputtering technique [26].	25
Figure 4.3 : Illustration of the magnetron sputtering process [27].	26
Figure 4.4 : Resistive evaporation method [28].	27
Figure 4.5 : Electron beam evaporation technique [2].	28
Figure 5.1 : The coating system.	31
Figure 5.2 : 3D topography of single-layer Al_2O_3 coatings with average R_a = (a) 2.98 nm, (b) 1.23 nm, and (c) 1.22 nm.	36
Figure 5.3 : 3D topography of single-layer Y_2O_3 coatings with average R_a = (a) 1.77 nm, (b) 0.60 nm, and (c) 1.02 nm.	37
Figure 5.4 : 3D topography of single-layer SiO_2 coatings with average R_a = (a) 1.05 nm, and (b) 0.72 nm.	37
Figure 5.5 : Transmittance (a) and reflectance (b) of 100 nm single-layer modeling for different materials.	39
Figure 5.6 : Transmittance (a) and reflectance (b) of 50 nm single-layer modeling for different materials.	40
Figure 5.7 : Thickness - wavelength - transmittance - reflectance relation of various single-layer thin film materials.	41
Figure 5.8 : Measured and simulated transmission values of (a) 136 nm, and (b) 69 nm Al_2O_3 films.	42
Figure 5.9 : Measured and simulated transmission values of (a) 130 nm, and (b) 73 nm Y_2O_3 films.	42
Figure 5.10 : Measured and simulated transmission values of (a) 120 nm, and (b) 69 nm SiO_2 films.	43
Figure 5.11 : Multilayer modeling of SiO_2 - h-BN combination.	45
Figure 5.12 : Multilayer modeling of Al_2O_3 - Y_2O_3 combination.	45
Figure 5.13 : Multilayer modeling of Ga_2O_3 - ZrO_2 combination.	46
Figure 5.14 : Multilayer modeling of three materials combination.	47
Figure 5.15 : Transmittance and reflectance of multilayer $\text{SiO}_2(70\text{nm})$ - $\text{Al}_2\text{O}_3(110\text{nm})$ coating, $N=4$.	48
Figure 5.16 : Transmittance and reflectance of multilayer $\text{Al}_2\text{O}_3(50\text{nm})$ - $\text{Y}_2\text{O}_3(75\text{nm})$ coating, $N=5$.	48

Figure 5.17: Transmittance and reflectance of multilayer $\text{SiO}_2(70\text{nm})$ - $\text{Al}_2\text{O}_3(110\text{nm})$ coating, $N=7$	48
Figure 5.18: Transmittance and reflectance of multilayer $\text{SiO}_2(130\text{nm})$ - $\text{Al}_2\text{O}_3(120\text{nm})$ coating, $N=10$	49
Figure 5.19: Transmittance and reflectance of $\text{Al}_2\text{O}_3(50\text{nm})$ - $\text{Y}_2\text{O}_3(75\text{nm})$ thin film notch filter, $N=15$	49
Figure 5.20: Transmittance and reflectance of multilayer $\text{SiO}_2(70\text{nm})$ - $\text{Al}_2\text{O}_3(110\text{nm})$ thin film notch filter, $N=15$	50
Figure 5.21: Absorptance of produced thin film notch filters (a) $\text{Al}_2\text{O}_3(50\text{nm})$ - $\text{Y}_2\text{O}_3(75\text{nm})$, and (b) $\text{SiO}_2(70\text{nm})$ - $\text{Al}_2\text{O}_3(110\text{nm})$	50
Figure 5.22: Transmittance of fabricated Al_2O_3 - Y_2O_3 thin film notch filter, $c_\lambda = 480 \text{ nm}$	52
Figure 5.23: Transmittance of fabricated SiO_2 - Al_2O_3 thin film notch filter, $c_\lambda = 620 \text{ nm}$	52
Figure 5.24: Transmittance of fabricated SiO_2 - Al_2O_3 thin film notch filter, $c_\lambda = 840 \text{ nm}$	53

SIMULATION AND FABRICATION OF THIN FILM NOTCH FILTER

SUMMARY

Optical filters are used for altering the optical properties of surfaces. They work on a specific range of the electromagnetic spectrum, and they are divided into two as interference and absorptive filters. Interference filters are composed of multilayer periodic thin films and they based on the interference principle of electromagnetic waves. In interference filters, desired transmission and reflection ratios can be achieved by controlling film thickness and refractive index of film material and substrate. There are many parameters of the refractive index, but the wavelength is the most outstanding one for optical filters. The wavelength-dependent refractive index is named dispersion and it can be expressed semi-empirical or empirical models. There are many types of interference filters, so they are categorized according to filtering shape and their location on the electromagnetic spectrum. Notch filters are a type of interference filter. Notch filters block a narrow band between the cut-off frequencies and they transmit other parts of the spectrum. They are the most complex interference filter type because of having two cut-off frequencies and a narrow non-transmitting band.

In this thesis, the main purpose is to create an open-source and free thin film notch filter simulation and fabricate various thin film notch filters using unused material combinations according to outputs of the simulation. Also, produced thin film notch filters are suitable for different applications. The thin film notch filter simulation has been created using Python software. The physical principles of the thin films are also in the scope of this thesis.

The most common way to produce optical thin films is the physical vapor deposition technique. The desired filters have been produced for the different ranges of the electromagnetic spectrum. During the experimental studies, three-set thin film notch filters have been manufactured whose center wavelength is 480 nm, 620 nm, and 840 nm; moreover, they can be used in various areas that are listed as neurobiology, Raman spectrometers, and infrared spectrometers, respectively.

Three dielectric materials, Al_2O_3 , Y_2O_3 , and SiO_2 , have been selected for manufacturing thin film optical filters, they have been composed of binary combinations of them. Previously simulated multilayer thin film notch filters have been fabricated using the electron beam evaporation technique. The electron beam evaporation method is a type of physical vapor deposition technique. Before manufacturing targeted notch filters, single-layer coatings have been designed and produced for comparison.

The thickness monitoring part of the coating system which calculates the coating thickness and deposition rate during the coating procedure, simultaneously, has been calibrated using measured film thickness of single-layer coatings. A film thickness of single-layer coatings has been measured using the surface profiler. Then, the thickness

monitoring unit has been calibrated using measured and calculated film thickness and mass density of the coating material. After the calibration, absolute film thickness deviation between the simulation and experiment has been calculated less than 10%. The reasons for the deviation percentage have been thought of as small changes in the dispersion equations of the coating materials, sensitivity of surface profiler, and calibration thickness monitoring system.

Moreover, film thickness and deposition rate effects on the surface roughness for each coating material have been investigated by atomic force microscopy since high surface roughness may cause undesired optical features due to the scattering of incoming light. As a result, the optimum deposition rate for multilayer stacks has been decided as 4.0 - 5.0 Å/s according to atomic force microscopy measurements.

Optical measurements of both single-layer and multilayer structures have been done by spectrophotometer. While the transmission rate of single-layer coatings had been comparing, the difference between simulated and measured values have been recognized in terms of amplitude. The amplitude difference in transmittance depends on neither film material nor thickness of the film. The difference is dimensionless, and it equals to approximately 1.52. After the compressive literature surveying, the constant has existed as a normalization parameter, and it has been stated as the refractive index ratio of the substrate and air. This normalization constant has been called a β parameter, and it has been used in the simulation of the multilayer thin film notch filters.

Numerically modelled multilayer thin film notch filters have been produced with different layer numbers after achieving adequate consistency between the simulation and experimental results. Transmittance, reflectance, and absorptance properties of produced multilayer thin film notch filters have been investigated in detail; besides the effect of layer number on the filter behavior has been examined.

Keywords: Interference Filter, Notch Filter, Thin Film, Optical Coating, Physical Vapor Deposition Techniques, Electron Beam Evaporation, Transmission, Simulation, Python

İNCE FİLM OPTİK EKSİLTME FİLTRE BENZETİMİ VE ÜRETİMİ

ÖZET

Optik filtreler yüzeylerin optik özelliklerini istenilen düzeyde kontrol edilmesi amacıyla kullanılan yapılardır. Elektromanyetik spektrumun çeşitli bölgelerinde çalışırlar ve girişim ve soğurma filtreleri olarak iki ana gruba ayrılmaktadırlar. Soğurma filtrelerinde temel olarak altlık malzemesine organik veya inorganik malzemelerin eklenmesiyle arzu edilen dalgaboyu aralığının soğurulması sağlanır. Girişim filtreleri ise soğurma filtrelerine kıyasla daha karmaşık yapılardır ve elektromanyetik dalgaların birbiri ile yaptıkları girişimlerin kontrolü prensibine dayanarak çalışır. Girişim filtreleri optik ince film kaplamayla üretilmektedir.

Filtre yüzeyine gelen ışınlar belirli bir oranda ince film yüzeyinden ve film tabakası altında yer alan altlıktan yansımaya uğrar. Yansıyan ışıklar arasında film kalınlığı ve film malzemesinin kırıcılık indisine bağlı olarak bir optik yol farkı oluşur. Optik yol farkı yansıyan elektromanyetik dalgalar arasında faz farkının oluşmasını sağlar. Böylece yapıcı ve yıkıcı girişimler meydana gelir. Yapıcı ve yıkıcı girişimlerin hassas kontrolü ile hedeflenen dalgaboyu aralığında filtre davranışı elde edilebilmektedir. Girişim filtreleri çok katmanlı genellikle periyodik olan ince film yapılardır. Girişim filtresinin karakteristiği film malzemelerinin kalınlığına, film malzemelerinin ve altlığın kırıcılık indisine ve periyodik katman sayısına bağlıdır. Girişim filtreleri de kendi içerisinde filtreleme şekline ve elektromanyetik spektrumda bulunduğu bölgelere göre sınıflandırılmıştır. Bunlardan en çok öne çıkanlar; monokromatik, uzun bant, kısa bant, optik eksiltme (notch), kenar, mor ötesi, kızıl ötesi filtrelerdir. Bir girişim filtre türü olan optik eksiltme filtreler, elektromanyetik spektrumda merkez bir dalgaboyunu ve komşuluğundaki dar bir bant aralığını geçirmeyen, spektrumun diğer bölgelerine karşılık gelen fotonların geçmesine için veren filtrelerdir. İki adet kesme frekansına sahip oldukları ve dar bir bant aralığında çalıştıkları için optik eksiltme filtreler girişim filtreleri arasında en karmaşık yapılardır. Filtreleme bandı o dalgaboyu aralığına karşılık gelen elektromanyetik dalgaların yapıcı girişim yapması sağlanarak ayarlanır. Girişim filtreleri ince film kaplama yöntemleriyle üretilmektedir.

Bu tezin temel amacı, Python yazılımı kullanılarak sık kullanılan ve daha önce kullanılmamış ince film malzeme birleşimleriyle özgün ince film optik eksiltme filtre benzetimi oluşturmak ve benzetim sonuçlarına göre çeşitli uygulamalarda kullanılmak üzere ince film optik eksiltme filtreler üretmektir. Benzetim sonuçlarıyla tutarlı olarak, merkez dalgaboyu 480 nm, 620 nm ve 840 nm olan farklı katman sayılarıyla üç set ince film optik eksiltme filtre üretilmiştir. Üretilen filtreler, nörobiyoloji, Raman spektrometreleri, kızılötesi spektrum uygulamalarında kullanılmaya uygundur. İnce film kaplama işlemi için en yaygın metot fiziksel buharlaştırma tekniğidir. Bu çalışmada üretilmesine karar verilen çok katmanlı ince film optik eksiltme filtreler bir fiziksel buharlaştırma tekniği türü olan elektron demeti buharlaştırma metodu kullanılmıştır.

Çalışma kapsamında ilk detaylı olarak ince filmlerin optik davranışını belirleyen fiziksel ilkeler belirlenerek gerekli matematiksel çıkarımlar yapılmıştır. Optik özellikleri belirleyen etmenler incelenerek benzetim matematiksel olarak ifade edilmiştir. Çalışma içerisinde detaylı anlatılan fiziksel prensiplerine dayanarak oluşturulan sayısal modelleme içerisinde bir malzeme kütüphanesi oluşturulmuştur. Benzetim programı içerisindeki malzeme kütüphanesindeki ince film malzemelerine ait olan dalgaboyuna bağlı optik kırıcılık fonksiyonları yer almaktadır. Kırılma indisine etki eden pek çok etmen vardır ancak gelen ışığın dalgaboyu en belirgin olanlardandır. Kırılma indisinin dalgaboyuna bağlılığı dağınım olarak adlandırılır ve malzemenin türü ve faz yapısına göre çeşitli dağınım yaklaşımları vardır. Saydam ve inorganik malzemeler için en tutarlı dağınım yaklaşımı; yarı deneysel bir yaklaşım olan Sellmeier dağınım eşitliğidir. Bu nedenle malzeme kütüphanesine belirlenen malzemelerin Sellmeier dağınım fonksiyonları literatürden eklenmiştir. Malzeme veri tabanı istenildiği takdirde her türden malzeme eklenerek kolaylıkla genişletilebilmektedir. Bu özelliği nedeniyle oluşturulan Python yazılımı limitsiz bir malzeme birleşimi imkânı sunmaktadır. Daha önce benzetimi veya üretimi yapılmamış malzeme birleşimleriyle özgün ince film optik eksiltme filtreleri elde etmek mümkün hale gelmiştir. Ücretsiz ve açık kaynak kodlu bir Python yazılımı oluşturulduğu için diğer bilim insanlarının erişmesi ve malzeme kütüphanesini genişleterek optik filtre benzetimi yapmaları mümkündür. Oluşturulan benzetim programı kullanılarak spektrumun farklı bölgelerinde, çeşitli malzeme istifleri ve tabaka kalınlıklarıyla çok sayıda ince film optik eksiltme filtreler sayısal olarak modellenmiş ve incelenmiştir.

İnce film kaplama tekniği olarak kullanılan elektron demeti buharlaştırma yöntemi, elektronların kinetik enerji transferi prensibine dayanmaktadır. Tungsten filamana alternatif akım uygulanarak elde edilen serbest elektronlar uygulanan yüksek potansiyel ile hızlandırılır ve yüksek vakum ortamında yüksek kinetik enerjiye sahip olurlar. Yüksek enerjili serbest elektronlar elektromıknatıslar sayesinde pota içerisindeki kaplama malzemesi üzerine düşürülür. Doğru akım olan sürüm akımının yavaşça artırılmasıyla elektronların sahip olduğu kinetik enerji, çarpışma etkisiyle kaplama malzemesine aktarılır ve katı haldeki film malzemesi buharlaşarak veya süblimleşerek gaz fazına geçer. Pota üzerinde yer alan altlık üzerinde birikmeye başlar. Anlık birikme hızı ise sistem içerisindeki kristal kalınlık görüntüleme sistemi ile hesaplanır. Sistem içerisindeki dönebilen pota tutucu 4 cc'lik altı adet pota yuvasına sahip olduğu için farklı film malzemelerinden oluşan çok katmanlı yapıların üretimi altlık tutucunun döndürülmesiyle mümkündür.

Üretim aşaması için ince film kaplamalarda kullanılmak üzere Al_2O_3 , Y_2O_3 ve SiO_2 dielektrik malzemeleri seçilmiştir. Kaplama malzemeleri belirlenirken bileşiklerin erişilebilirliği, saydamlık aralığı ve birbirlerine göre kırıcılık indis farkları göz önünde bulunduruldu. Üretimi planlanan merkez dalgaboyu 480 nm, 620 nm ve 840 nm olan çok katmanlı optik eksiltme filtreler sırasıyla farklı film kalınlıklarındaki Al_2O_3 - Y_2O_3 , Al_2O_3 - SiO_2 ve Al_2O_3 - SiO_2 malzeme çiftleri kullanılarak oluşturulan Python yazılımında benzetilmiştir. Çok katmanlı yapılar üretilmeden önce, seçilen her bir malzeme iki farklı kalınlıkta tek katman olarak altlık olarak belirlenen corning cam üzerine biriktirilmiştir. Tek katmanlı yapılar kullanılarak kaplama sisteminin kalınlık görüntüleme bölümü kalibre edilmiştir. Ayrıca Python benzetim yazılımı da ölçülen deneysel veriler ışığında düzeltilmiştir. Film kalınlıkları yüzey profilometresi ile ölçülmüştür. Kaplama malzemesinin gerçek kalınlığı ve kütle yoğunluğu kullanılarak kalınlık görüntüleme sistemi kalibre edilmiştir. Daha sonra benzetim programı ve

deneysel örneklerin geçirgenlik oranları karşılaştırılarak film kalınlığındaki sapma oranı %10'dan daha az olarak hesaplanmıştır. Geçirgenlik ve yansıtma ölçümleri spektrofotometre cihazı ile yapılmıştır. Bu sapmaların sebepleri film malzemesinin Sellmeier dağınım eşitliğindeki küçük değişimler, yüzey profilometresinin ölçüm hassasiyeti ve kalınlık görüntüleme sisteminin sapmaları olarak düşünülmektedir. Ayrıca tek katmanlı kaplamaların geçirgenlik ölçümü ile benzetim programı ile elde edilen değerin şiddetinde belirli bir farklı olduğu anlaşılmıştır. Bu farklılığın kaplamanın malzeme tipinden ve kalınlığından bağımsız olduğu görülmüştür. Yapılan detaylı araştırma sonucu bu farklılığın boyutsuz bir sabit olduğu ve yaklaşık 1.52 gibi bir değere eşit olduğu fark edilmiştir. Daha sonra bu değerin bir normalizasyon terimi olduğu ve altlığın kırılma indisinin havanın kırılma indisine oranı olduğu tespit edilmiştir. Bu orana β terimi adı verilerek benzetim programı modifiye edilmiştir. Daha sonra çok katmanlı yapıların benzetimi yapılırken geçirgenlik değeri boyutsuz β katsayısı ile çarpılarak hesaplanmıştır. Böylece sayısal modellemenin çıktıları, deneysel ölçümlerle daha tutarlı bir hale gelmiştir.

Ek olarak tek katmanlı kaplamalar atomik kuvvet mikroskopu ile incelenerek film kalınlığı ve biriktirme hızının yüzey pürüzlülüğüne etkisi araştırılmıştır. Çünkü film tabakasındaki yüzey pürüzlülüğü gelen ışığın saçılmasına neden olarak arzu edilen optik özelliklerin elde edilmesini engelleyebilir. Yapılan deneysel incelemenin ardından üretilecek çok katmanlı ince film optik eksiltme filtreleri için uygun biriktirme hızı 4.0 – 5.0 Å/s olarak belirlenmiştir.

Benzetim ve deneysel sonuçlar arasında yeterli tutarlığa ulaşıldıktan sonra hedeflenen çok katmanlı ince film optik eksiltme filtreleri farklı katman sayılarıyla modellenmiştir. Daha sonra elektron demeti buharlaştırma sistemi kullanılarak üç farklı katman sayısında üretilmiştir. Üretilen çok katmanlı ince film optik filtrelerin tüm optik özellikler detaylı olarak incelenerek geçirgenlik ve yansıtma oranları ölçülmüş ve soğurma oranı hesaplanmıştır. Bu inceleme sonucu optik eksiltme filtrenin çalıştığı dar bant aralığında geçmesini engellediği elektromanyetik dalgaları soğurduğu görülmüştür. Soğurma oranının periyodik ince film katman sayısı ile arttığı belirlenmiştir. Ek olarak, her bir filtre için periyodik katman sayısının filtre davranışına olan etkisi incelenmiştir. Periyodik katman sayısı arttıkça optik eksiltme filtrenin davranışının keskinleşerek geçirgenliğin sıfıra yakınsadığı görülmüştür.

Anahtar Kelimeler: Girişim Filtresi, Notch Filtre, Optik Eksiltme Filtresi, İnce Film, Optik Kaplama, Fiziksel Buharlaştırma Tekniği, Elektron Demeti Buharlaştırma, Geçirgenlik, Simülasyon, Benzetim, Python



1. INTRODUCTION

1.1 Historical Background of Light: Wave-Particle Duality

Photon, namely light, is one of the most complex phenomena in modern physics because of its dual nature. The scientific history of the wave-particle duality of light dates back to 5th century BC. At that time, Democritus discussed those entire elements of the universe and he concluded that everything in the universe, including light, consists of indivisible sub-particles. He called these tiny components as atoms. Euclid (3rd century BC) and Ibn-i Al Haytam (11th century) who wrote the first comprehensive optics book in history investigated propagation and reflection phenomena of a light beam. They claimed that light beams were composed of light particles.

Besides, Isaac Newton studied the behavior of light in the 16th century, and his observations had provided extensive perspective to scientists especially on colored reflections of light. The following contributors to the optical behavior of light were Robert Hooke, Thomas Young, Augustine Jean Fresnel, and Christiaan Huygens. Fresnel and Huygens completed a mathematical explanation of wave propagation of light successfully, and the double-slit experiment of Young was supported the theoretical results [1]. In the 19th century, James Clerk Maxwell proved changing the electrical field induces a magnetic field in Ampere's law. After this modification, it was discovered that light is an electromagnetic wave according to four Maxwell equations. Consequently, all types of light such as; ultraviolet, visible and infrared are electromagnetic waves of different wavelengths on the electromagnetic spectrum.

After a wave-like approach of light, Max Planck and Albert Einstein showed the particle-like nature of photon as a result of their works which are black body irradiation and the photoelectric effect, respectively in the 20th century. Around the same time, contemporary of Planck and Einstein, Louis Victor De Broglie demonstrated wave-like behavior of light experimentally. Nowadays, there is no doubt that light in other words

photon or electromagnetic radiation has wave-particle duality. A thin film phenomenon of optics is based on the wave-like attitude of light.

First studies on thin film phenomena were done in the middle of the 17th century by Jan Marek Marci, Robert Boyle, Francesco Maria Grimaldi, and Robert Hooke. They tried to comprehend the reason of colored reflections from daily occasions such as soap bubbles, oil slicks [2]. Nevertheless, their works did not sufficient to describe these natural situations. After the elaborately studies of Augustine Jean Fresnel and Thomas Young, it was understood that interference of electromagnetic waves is the fundamental physical reason of colored reflections in nature [3]. Following this discovery, many scientists contributed to improving the physical principles of optics and the design of optical coatings. However, the fabrication of optical coating was not succeeded until the beginning of the 20th century due to a lack of technology.

1.2 Optical Filters

Production of thin film coating has been become achievable throughout of improvement in vacuum technology in the 1930s. In the following decades, thin film filters were fabricated by developing both vacuum and deposition technology [2]. Consequently, optical filter technology has enhanced and started to spread in numerous areas.

Today, optical filters have become more sophisticated and high-quality. They are commonly used in different areas; they also, have a crucial role in specific applications such as; defense industry, neuroscience, various spectroscopies, glass technology, and optical lenses. Optical properties of a surface like; transmission, reflection, and absorption can be altered using an optical filter. These three optical characteristics are tunable for desired applications. The variety of optical filters consists of their operating principle and working region on the electromagnetic spectrum. There are two main optical filter types according to the working principle: absorptive and interference filters.

1.2.1 Absorptive filters

Absorptive filters generally block a certain part of the electromagnetic spectrum while they allow transmitting other wavelengths. The blocked part is the unwanted

wavelengths to transmit. This part mostly takes place on the visible and infrared region of the spectrum according to the application area. This type of filter is produced by adding organic or inorganic compounds to the substrate [4]. In some applications, polycarbonate and acrylic matrix are preferable, so the filter structure becomes lighter. The working region of a filter on the spectrum depends on the type of adding substance. The amount of adding material determines the absorption ratio of the filter [5].

1.2.2 Interference filters

Interference filters, known as dichroic filters are more complex optical filters than absorptive ones. The working principle of the dichroic filter is based on the interference phenomenon in optics. The basic description of the interference principle is if two incident electromagnetic waves from the parallel surfaces in phase, they are interfering constructively. In this condition, the optical path difference between two light waves equals an exact multiple of the wavelength. Unlike, if the two electromagnetic waves coming from parallel surfaces are out of phase, they destructively interfere. In this situation, odd multiple of wavelength or one-half of it is equal to the optical path difference between the waves [6].

Transmittance – reflectance ratio of a filter can be adjusted by using the interference principle. To utilize this phenomenon, the surface is coated with thin films. The thin film can be coated by physical vapor deposition (PVD) and chemical vapor deposition (CVD) techniques properly. However, fabrication of interference optical filters is more expensive than the manufacturing of absorptive filters due to the cost of PVD and CVD techniques.

The optical behavior of the dichroic filter depends on the number of coating layers and their thicknesses. Thin film filter can consist of from one to dozens of layers [7]. It is possible to control transmittance and reflectance as a function of wavelength in the desired spectral region by changing the number of layers, thickness of each layer, coating material, and substrate. Today, there are numerous types of interference filters depending on the variety of these parameters. Filter types are classified according to their operating shape and working region name of the electromagnetic spectrum (Figure 1.1) [8].

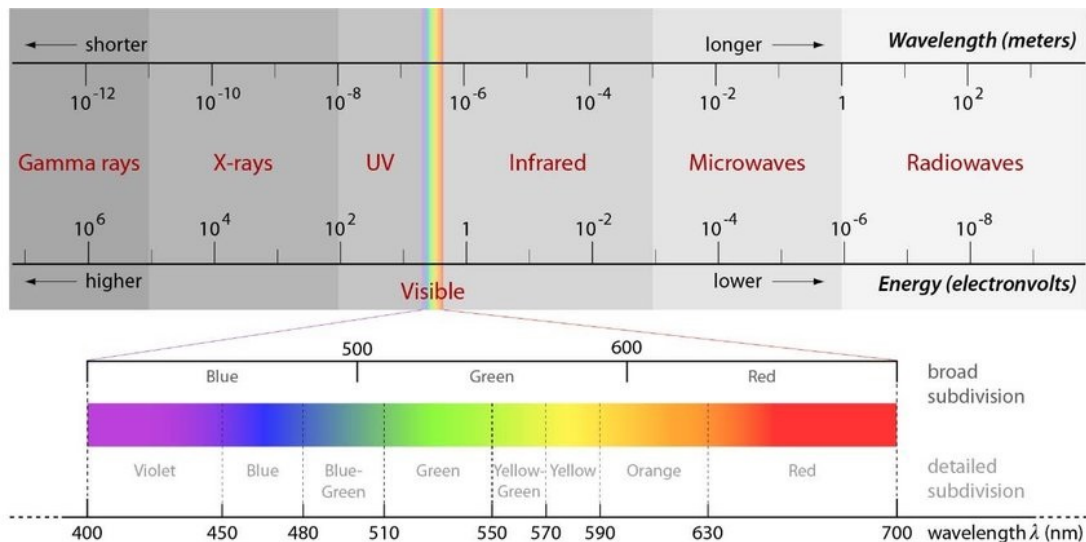


Figure 1.1 : Electromagnetic spectrum [8].

For instance, monochromatic filters work on the visible region of the spectrum and they transmit particular bandwidth. This band corresponds to one color. Ultraviolet filters are used for blocking ultraviolet radiation. This type of filter is used in the photography field to obtain a better resolution. Similarly, infrared filters allow passing the whole spectrum waves except the infrared region. They are used to prevent overheating of electronic systems and buildings caused by sun rays. Another type of dichroic filters is edge filters. This type of filter has one cut off frequency. It transmits higher wavelengths and reflects shorter ones from the cut off frequency. This type of filter named as a high-pass filter. With the same logic, an optical filter that transmits a shorter wavelength spectrum than its cut off frequency is called a short-pass filter. High-pass filters and short-pass filters are used for fluorescence microscopy and microspectrometers [9] [10]. A thin film notch filter is the most complex one in optical filters because it has two cut off frequency. This type of filter blocks to transmit a narrow spectral region between the cut off frequencies. The region of the filter behavior depends on constructive interferences. Notch filters have varied application areas such as sensors, infrared cameras, spectroscopies, and neuroscience.

For example, Raman spectrometers need notch filter that used for blocking laser beams having 514 nm inside the device in order to avoid noises during the measurement [4]. The wavelength of the beams is characteristic of the laser source material. The characteristic wavelength of laser beam source materials is ranging from 470 nm to 530 nm, typically.

Migraine and photophobia sufferers have abnormal sensitivity toward the daylight. Light can trigger a migraine and photophobia attack in their daily life. Hoggan et al. studied the effect of wearing 480 nm and 620 nm optical notch filter lenses on the chronic-migraine or photophobia sufferers. They selected these two wavelengths because the human eye is highly sensitive in that band. The result of that study is hopeful for the treatment of chronic-migraine and photophobia [11].

1.3 The Content of Study

In the present study, it has been aimed to model thin film notch filters mathematically by Python programming language. It is expected that simulation achieves notch filter behavior in the different regions of the electromagnetic spectrum using refractive index parameters of different materials. Then, it has been planned to fabricate three-set thin film notch filters according to the simulation result. The study is unique in terms of the use of previously unused materials combinations during the production of notch filters for different regions of the spectrum.

The consistency between experimental and calculated results is crucial for the study. Fabricated thin film notch filters can be used for Raman and infrared spectroscopies and treatment of chronic migraine and photophobia.

In chapter 2, the physical principles of the thin film have been studied. The basic theory about the optical behavior of thin films has been mathematically explained. Besides, the parameters of optical properties have been mentioned.

The numerical modeling of both single-layer and multilayer coatings has been introduced in chapter 3. Also, created materials database for simulation has been presented in this section.

Thin film coating techniques have been briefly explained in chapter 4. Working principles of the CVD method and types of PVD techniques have been presented with their operational requirements and units. The parts of the system have been introduced with their significant roles.

In chapter 5, all experimental procedures have been presented. Initially, the features of our thin film coating system have been explained. Whole optical properties of simulated coating structures have been given in this section and they have been

compared with characteristics of fabricated ones. The transmission correction of numerical and experimental results has been completed in this chapter. Performed characterization methods of single-layer and multilayer coatings have been also briefly explained and all results have been presented. Experimental results have been discussed in the end of this chapter.

Finally, the conclusion of the study has been presented in section 6.



2. OPTICAL BEHAVIOR OF THIN FILMS: PHYSICAL PRINCIPLES

2.1 Thin Film

As it is mentioned in the previous section, the physics behind the working principle of thin film optical filters is interference phenomena. The definition of a thin film is a layer of material whose thickness ranging from one atomic layer thickness to several μm . One atomic layer coatings are called as mono-layer coating, especially. The path of the incident electromagnetic wave on the surfaces of thin film and substrates is shown in Figure 2.1.

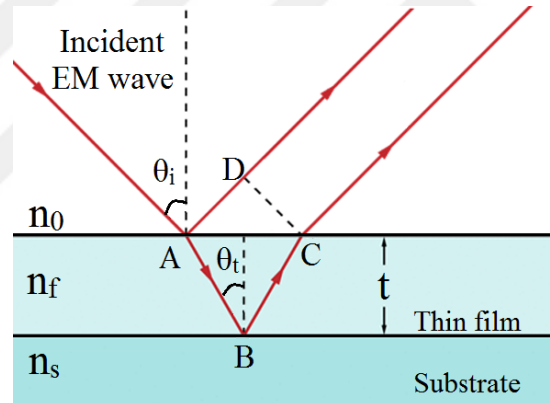


Figure 2.1 : The path of incident electromagnetic wave on surfaces.

Interference is based on the optical path difference between surfaces. The path difference of incoming light changes when it is reflected in different surfaces. This changing results in phase difference among reflected electromagnetic waves. The optical path difference, δ , can be calculated according to Figure 2.1 as

$$\Delta = (\overline{AB} + \overline{BC})n_f - (\overline{AD})n_0 \quad (2.1)$$

n_0 represents the refractive index of the medium which is generally air in many coatings. n_f and n_s are the refractive index of the thin film and the substrate, respectively. Δ can be modified after using geometric relations for Equation (2.1) as

$$\Delta = 2n_f t \cos \theta_t \quad (2.2)$$

In Equation (2.2), θ_t is the angle between normal and \overline{AB} , and t is equal to the thickness of the film. In the simulation step this angle has been calculated as 60° according to incident light angle of the spectrometer. When the optical path difference is multiplied with wave number, k , the phase difference (δ) is obtained.

$$\delta = k\Delta = (2\pi/\lambda)(2n_f t \cos \theta_t) \quad (2.3)$$

It can be understood from Equation (2.3) that if Δ is equal to wavelength (λ) of incident electromagnetic wave, δ proportional with 2π . In this situation, two waves are in phase after reflection. It means that constructive interference occurs between the electromagnetic waves. In contrast, if the optical path difference is equal to $\lambda/2$, the phase difference between the waves equals π . Consequently, two waves are out of phase after the reflections, and it results in destructive interference.

In conclusion, the interference phenomena of the thin film depend on the wavelength of incoming light, thickness and refractive index of the film.

2.2 Optical Basics

Since the wave-like behavior of light is handled in optical thin films, Maxwell equations in electrodynamics can be used for mathematical derivations of optical parameters. Maxwell equations are introduced in Equations (2.4) – (2.7).

$$\nabla \cdot \vec{E} = \frac{\rho}{\epsilon_0} \quad (2.4)$$

$$\nabla \cdot \vec{B} = 0 \quad (2.5)$$

$$\nabla \times \vec{E} = -\frac{\partial \vec{B}}{\partial t} \quad (2.6)$$

$$\nabla \times \vec{B} = \mu_0 \vec{J} + \mu_0 \epsilon_0 \frac{\partial \vec{E}}{\partial t} \quad (2.7)$$

Where \vec{E} and \vec{B} are electrical and magnetic field vectors, and μ_0 and ϵ_0 permittivity and permeability of space, respectively. \vec{J} is the current density vector, and ρ is charge

density. When the Equations (2.6) and (2.7) are resolved together, the magnetic field in the medium is obtained in terms of the electrical field (Equation (2.8)) [12].

$$B = \frac{1}{v}E \quad (2.8)$$

It is known that $v = \frac{c}{n}$, and $c = \frac{1}{\sqrt{\mu_0\epsilon_0}}$. v and c are speed of light in the medium and space, respectively. Both magnetic and electric field magnitudes are obtained in terms of refractive index.

$$B = n\sqrt{\mu_0\epsilon_0}E \quad (2.9)$$

After the understanding relation between fields, electric and magnetic field components of light on the thin film surface can be calculated. Figure 2.2 shows the reflection and transmission of incident light from a single-layer thin film [13]. In the present work, the notations in Figure 2.2 will be used while obtaining the transition matrix of the thin films by calculating the electric and magnetic fields.

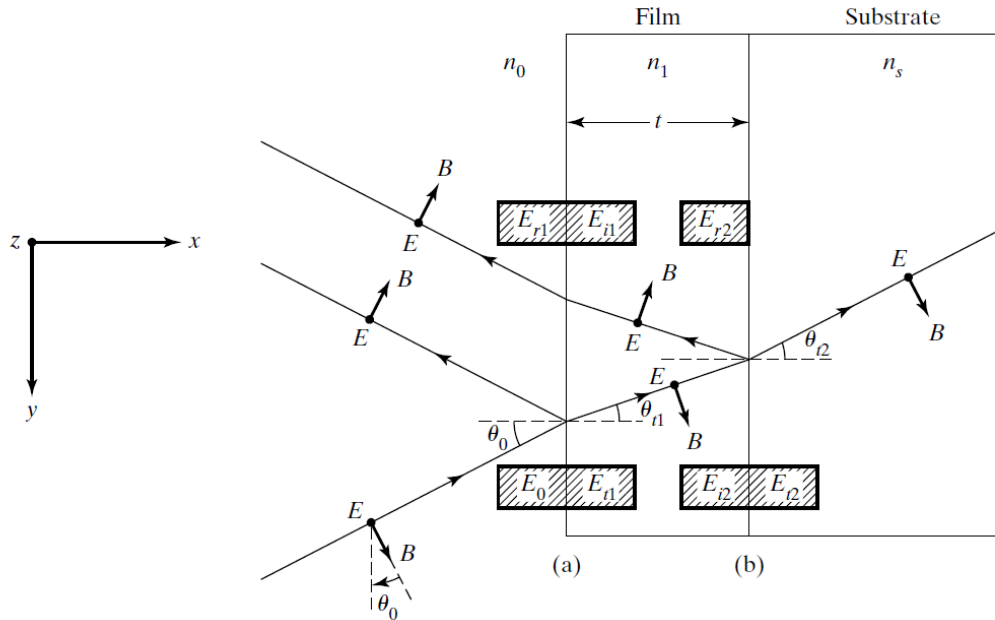


Figure 2.2 : Transmission and reflection from the single-layer thin film [13].

According to Figure 2.2, the E component of the incident electromagnetic wave is chosen to be perpendicular to the plane with a reflected part of the wave and the normal. The beam from the first surface of the thin film facing air (a) undergoes external reflection. The part of the beam that passes into the film undergoes a second

internal reflection on the back surface (b) of the film that separates the film from the substrate and passes to the bottom. The direction of the electric field component of the beams in the air, in the film and the substrate medium is outward from the sheet (in the z-direction). The direction of the magnetic field components (B) of the beams is as shown in the figure. During reflection, the magnetic field (B) y component is directed opposite.

Moreover, boundary conditions should be written for electric and magnetic fields which are composed of planar waves encountering surfaces (a) and (b). According to the electromagnetic theory, the components of the electric and magnetic fields parallel to the surfaces must be continuous, that is, the component intensities must be equal on both sides of the intersection. According to the specified notation, the electric field is parallel to the surface at each point of the surfaces (a) and (b), but the magnetic field consists of both components parallel to the surface (in the y-direction) and perpendicular to the surface (in the x-direction).

Electric and magnetic fields in air, thin film and substrate interfaces according to the boundary conditions of an electromagnetic theory are below as

$$E_a = E_0 + E_{r1} = E_{t1} + E_{i1} \quad (2.10)$$

$$E_b = E_{i2} + E_{r2} = E_{t2} \quad (2.11)$$

$$B_a = B_0 \cos \theta_0 - B_{r1} \cos \theta_0 = B_{t1} \cos \theta_{t1} - B_{i1} \cos \theta_{t1} \quad (2.12)$$

$$B_b = B_{i2} \cos \theta_{t1} - B_{r2} \cos \theta_{t1} = B_{t2} \cos \theta_{t2} \quad (2.13)$$

Equations (2.14) and (2.15) can be calculated by combining the relationship between magnitudes of electric and magnetic fields (Equation (2.9)) and Equation (2.12) – (2.13).

$$B_a = n_0 \sqrt{\mu_0 \epsilon_0} \cos \theta_0 (E_0 - E_{r1}) = n_1 \sqrt{\mu_0 \epsilon_0} \cos \theta_{t1} (E_{t1} - E_{i1}) \quad (2.14)$$

$$B_b = n_1 \sqrt{\mu_0 \epsilon_0} \cos \theta_{t1} (E_{i2} - E_{r2}) = n_s \sqrt{\mu_0 \epsilon_0} \cos \theta_{t2} (E_{t2}) \quad (2.15)$$

For simplicity, Equations (2.14) and (2.15) are rewritten in terms of gamma parameters.

$$B_a = \gamma_0 (E_0 - E_{r1}) = \gamma_1 (E_{t1} - E_{i1}) \quad (2.16)$$

$$B_b = \gamma_1(E_{i2} - E_{r2}) = \gamma_s(E_{t2}) \quad (2.17)$$

The gamma parameters in previous equations belong to air, the thin film and the substrate, respectively.

$$\gamma_0 = n_0 \sqrt{\mu_0 \epsilon_0} \cos \theta_0 \quad (2.18)$$

$$\gamma_1 = n_1 \sqrt{\mu_0 \epsilon_0} \cos \theta_{t1} \quad (2.19)$$

$$\gamma_s = n_s \sqrt{\mu_0 \epsilon_0} \cos \theta_{t2} \quad (2.20)$$

These three gamma parameters have a crucial role in obtaining the characteristic matrix of the thin film in the next calculations.

If the magnetic field vector is chosen perpendicular to the incoming plane instead of the electric field vector, the cosine parameter in the term γ_1 takes place in the denominator instead of the numerator. So

$$\gamma_1 = n_1 \frac{\sqrt{\mu_0 \epsilon_0}}{\cos \theta_{t1}} \quad (2.21)$$

Under these boundary conditions, if E_{t1} and E_{i1} are rewritten in terms of E_{t2} and E_{r2} , respectively, the following equations are obtained due to phase difference (according to Equation (2.3)).

$$E_{i1} = E_{r2} e^{-i\delta} \quad (2.22)$$

$$E_{i2} = E_{t1} e^{-i\delta} \quad (2.23)$$

When Equations (2.22) and (2.23) are combined with Equations (2.11) and (2.13) at the boundary condition (b), electric and magnetic fields at (b) are obtained as

$$E_b = E_{t1} e^{-i\delta} + E_{i1} e^{i\delta} = E_{t2} \quad (2.24)$$

$$B_b = \gamma_1(E_{t1} e^{-i\delta} - E_{i1} e^{i\delta}) = \gamma_s E_{t2} \quad (2.25)$$

Using the equations above, E_{t1} and E_{i1} are calculated as function of E_b and B_b .

$$E_{t1} = \left(\frac{\gamma_1 E_b + B_b}{2\gamma_1} \right) e^{i\delta} \quad (2.26)$$

$$E_{i1} = \left(\frac{\gamma_1 E_b - B_b}{2\gamma_1} \right) e^{-i\delta} \quad (2.27)$$

If E_{t1} and E_{i1} are resolved according to Equations (2.10) and (2.12) to satisfy the boundary conditions, both electric and magnetic field equations on (a) are calculated.

$$E_a = \left(\frac{\gamma_1 E_b + B_b}{2\gamma_1} \right) e^{i\delta} + \left(\frac{\gamma_1 E_b - B_b}{2\gamma_1} \right) e^{-i\delta} \quad (2.28)$$

$$= E_b \cos \delta + B_b \left(\frac{i \sin \delta}{\gamma_1} \right) \quad (2.29)$$

and

$$B_a = \left(\frac{\gamma_1 E_b + B_b}{2\gamma_1} \right) e^{i\delta} - \left(\frac{\gamma_1 E_b - B_b}{2\gamma_1} \right) e^{-i\delta} \quad (2.30)$$

$$= \frac{\gamma_1 E_b}{2} e^{i\delta} + \frac{B_b}{2} e^{i\delta} - \frac{\gamma_1 E_b}{2} e^{-i\delta} - \frac{B_b}{2} e^{-i\delta} \quad (2.31)$$

$$= i\gamma_1 E_b \left(\frac{e^{i\delta} - e^{-i\delta}}{2i} \right) + B_b \left(\frac{e^{i\delta} + e^{-i\delta}}{2} \right) \quad (2.32)$$

$$= i\gamma_1 E_b \sin \delta + B_b \cos \delta \quad (2.33)$$

Consequently, it can be seen that the electric field and magnetic field values on the surface (a) can be written in terms of the electric and magnetic field values on the surface (b). These equations can also be written in matrix form.

$$\begin{pmatrix} E_a \\ B_a \end{pmatrix} = \begin{pmatrix} \cos \delta & \left(\frac{i \sin \delta}{\gamma_1} \right) \\ \gamma_1 i \sin \delta & \cos \delta \end{pmatrix} \begin{pmatrix} E_b \\ B_b \end{pmatrix} \quad (2.34)$$

The 2×2 matrix which is shown Equation (2.34) is named as the characteristic matrix of the thin film. It can be generalized as

$$M = \begin{pmatrix} m_{11} & m_{12} \\ m_{21} & m_{22} \end{pmatrix} \quad (2.35)$$

In the multilayer thin film systems, the characteristic matrix of the system equals the multiplication of each thin film characteristic matrix.

To calculate transmission and reflection coefficients of the thin film, Equations (2.10), (2.11), (2.16), and (2.17) should be written in the characteristic matrix of the system.

$$\begin{pmatrix} E_0 + E_{r1} \\ \gamma_0(E_0 - E_{r1}) \end{pmatrix} = \begin{pmatrix} m_{11} & m_{12} \\ m_{21} & m_{22} \end{pmatrix} \begin{pmatrix} E_{t2} \\ \gamma_s E_{t2} \end{pmatrix} \quad (2.36)$$

The following equations are obtained from the matrix above.

$$E_0 + E_{r1} = m_{11}E_{t2} + m_{12}\gamma_s E_{t2} \quad (2.37)$$

$$\gamma_0(E_0 - E_{r1}) = m_{21}E_{t2} + m_{22}\gamma_s E_{t2} \quad (2.38)$$

The transmission coefficient (t) is defined as the ratio of transmitted light to incident light. So, it can be expressed mathematically as

$$t = \frac{E_{t2}}{E_0} \quad (2.39)$$

Similarly, the reflection coefficient (r) is the function of the reflected portion of incoming electromagnetic waves. It is equal to

$$r = \frac{E_{r1}}{E_0} \quad (2.40)$$

Transmission and reflection coefficients are obtained in terms of gamma parameters and elements of a characteristic matrix using Equations (2.38) and (2.37).

$$t = \frac{2\gamma_0}{\gamma_0 m_{11} + \gamma_0 \gamma_s m_{12} + m_{21} + \gamma_s m_{22}} \quad (2.41)$$

$$r = \frac{\gamma_0 m_{11} + \gamma_0 \gamma_s m_{12} - m_{21} - \gamma_s m_{22}}{\gamma_0 m_{11} + \gamma_0 \gamma_s m_{12} + m_{21} + \gamma_s m_{22}} \quad (2.42)$$

Transmittance (T) and reflectance (R) are equals to the multiplication of their coefficients and complex conjugates of them.

$$T = t^* t = |t|^2 \quad (2.43)$$

$$R = r^* r = |r|^2 \quad (2.44)$$

T ratio requires a normalization parameter. The correction of calculations and simulation will be stated in Chapter 5 after the investigation of single-layer coatings.

For non-absorbing structures: $T + R = 1$

However, absorptance (A) is taken into account in many coatings. Thus, the following equation is valid.

$$T + R + A = 1 \quad (2.45)$$

2.3 Parameters of Refractive Index

The refractive index is defined as the ratio of the velocity of electromagnetic radiation in one medium to that another one [14]. The speed of light varies according to the refractive index of materials. As stated in the previous section, one of the main parameters determining the optical features of the thin film filter is the refractive index of film, substrate, and medium. Many factors affect the refractive index in nature, but wavelength, mass density, temperature, and impurity are the most outstanding ones.

2.3.1 Wavelength

The propagation of electromagnetic radiation through a material is controlled by the permittivity and the permeability properties. It is known from optics that both features of materials depend on the frequency of light. The refractive index is composed of the permittivity and permeability [12].

$$n_i = \sqrt{\frac{\epsilon_i \mu_i}{\epsilon_0 \mu_0}} \quad (2.46)$$

μ_i is almost equal to μ_0 for many materials, so

$$n_i \cong \sqrt{\frac{\epsilon_i}{\epsilon_0}} \quad (2.47)$$

If these properties were independent of wavelength, the refractive index would become constant. Nevertheless, in this case, the refraction index becomes a function of wavelength. In physics, the wavelength dependence of the refractive index is called dispersion.

For gas molecules and medium, simplified Cauchy's dispersion formula can be written as

$$n_i = 1 + \frac{Nq^2}{2m_e\epsilon_0} \left(\sum_{j=1} \frac{f_j}{\omega_j^2 - \omega^2} \right) \quad (2.48)$$

where m_e is mass of an electron, q is the electrical charge of an electron, N is the number of atom/molecule, f_j is the number of the resonant electron in each state, ω is frequency.

$$\frac{1}{\omega_j^2 - \omega^2} = \frac{1}{\omega_j^2} \left(1 - \frac{\omega^2}{\omega_j^2} \right)^{-1} \cong \frac{1}{\omega_j^2} \left(1 + \frac{\omega^2}{\omega_j^2} \right) \quad (2.49)$$

when Equation (2.49) is written into Equation (2.48), the following equation is obtained.

$$n_i = 1 + \left(\frac{Nq^2}{2m_e\epsilon_0} \sum_{j=1} \frac{f_j}{\omega_j^2} \right) + \omega^2 \left(\frac{Nq^2}{2m_e\epsilon_0} \sum_{j=1} \frac{f_j}{\omega_j^4} \right) \quad (2.50)$$

and

$$\lambda = \frac{2\pi c}{\omega} \quad (2.51)$$

Cauchy's dispersion formula can be expressed in terms of wavelength when Equation (2.51) is written in Equation (2.50).

$$n_i = 1 + A \left(1 + \frac{B}{\lambda^2} \right) \quad (2.52)$$

A and B are constant and they are called the coefficient of refraction and dispersion, respectively. Cauchy's dispersion equation is quite useful for most gases [12]. There are several dispersion formulas except for Cauchy's formula. They are mostly empirical equations and they differ from each other using areas. For thin films and transparent glasses, the Sellmeier dispersion formula can apply reasonably [15]. The general formula of the Sellmeier dispersion equation is given below.

$$n_i^2 = A + \frac{B\lambda^2}{\lambda^2 - C^2} + \frac{D\lambda^2}{\lambda^2 - E^2} + \frac{F\lambda^2}{\lambda^2 - G^2} \quad (2.53)$$

where A , B , D , and F are dimensionless constant and the unit of C , E , and G is nm.

In the present study, the Sellmeier dispersion equation of chosen materials has been used during numerical modeling.

2.3.2 Mass density

Mass density is one of the main determinants of the refractive index because light propagates slower in dense material or medium. The refractive index increases linearly with increasing mass density until the 1 g/cm^3 . After this threshold value, linearity slightly disappears [16]. So, there is no linear relation between mass density and the refractive index for dense materials. Light tends to scatter relatively large from dense materials.

2.3.3 Temperature

Temperature dependence of the refractive index relates to mass density. It is well known that mass density decreases with increasing temperature because of thermal expansion. According to this logic, the refractive index decreases if temperature increases. The specific heat capacity of materials also determines the rate of this relation. The decrease in refractive index varies between 1×10^{-4} and 1×10^{-3} , depending on the material, in 1°C rise in temperature.

2.3.4 Impurity

Electromagnetic waves pass slower into heterogeneous regions in materials. Impurities disturb homogeneity in materials, so the refractive index increases. Also, defects in a material have the same effect on the refractive index.

3. NUMERICAL MODELING OF THIN FILM NOTCH FILTER

In this chapter, the simulation method of both single-layer and multilayer thin film structures will be introduced. During the numerical calculations, Python 3.0 and Jupyter Notebook were used. Several programs are available for thin film filter design using mandatory two materials; however, generally, they have two fundamental drawbacks.

They are not free programs and limited in terms of materials variety. In order to avoid these disadvantages, a basic and free program was created by using the software mentioned. The outstanding advantages of created simulation can be listed as the user is unrestricted in terms of material variety and control the structural characteristics of the thin film as desired. Thus, previously unused materials combinations can be performed. Besides, unique notch filter attitude can be achieved using more than two materials combinations.

The simulation works according to physical principles which have been explained in Chapter 2.

3.1 Material Selection

First of all, in order to simulate an optical behavior of a thin film notch filter by Python, creating a materials library is essential. This materials database should include the wavelength-dependent refractive index of film materials. Consequently, the Sellmeier dispersion equation of chosen materials has been embedded in the formed library.

In the literature, scientists have been produced thin film filters using mostly metal oxides in previous studies. In some cases, nitrides have been used also. Consequently, we decided that the materials library consists of both metal oxides and nitrides. Also, it includes previously non-used compounds.

TiO₂ [17], SiO₂ [18], ZrO₂ [19], Ga₂O₃ [20], Y₂O₃ [21], Al₂O₃ [22], AlN [23] and h-BN [24] have been selected for materials database and their dispersion formulas are

given in Table 3.1. Corning glass [25] has been determined as substrate due to its high quality optical features.

Table 3.1 : Chosen materials and their Sellmeier dispersion equations.

Material	A	B	C (nm)	D	E (nm)	F	G (nm)
$n_{TiO_2}^2$	5.913	494.0648	283.3726				
$n_{SiO_2}^2$	1	0.6962	68.4043	0.4079	116.2414	0.8975	9896.2
$n_{ZrO_2}^2$	1	3.3037	198.7971				
$n_{Ga_2O_3}^2$	3.5259	203.2486	173.2628				
$n_{Y_2O_3}^2$	1	2.578	138.71	3.935	22936		
$n_{Al_2O_3}^2$	1	1.4314	72.6631	0.6505	119.3242	5.3414	18028.3
n_{AlN}^2	3.1399	1.3786	171.5	3.861	15030		
n_{h-BN}^2	1	3.263	164.4				

Table 3.1 shows the Sellmeier dispersion equations of selected materials in the form of Equation (2.53). Eight compounds have been chosen for thin film notch filter design in the first step, but the materials database can be easily expanded for future studies if required. Figure 3.1 shows the wavelength-dependent refractive index of selected materials for material database of the model.

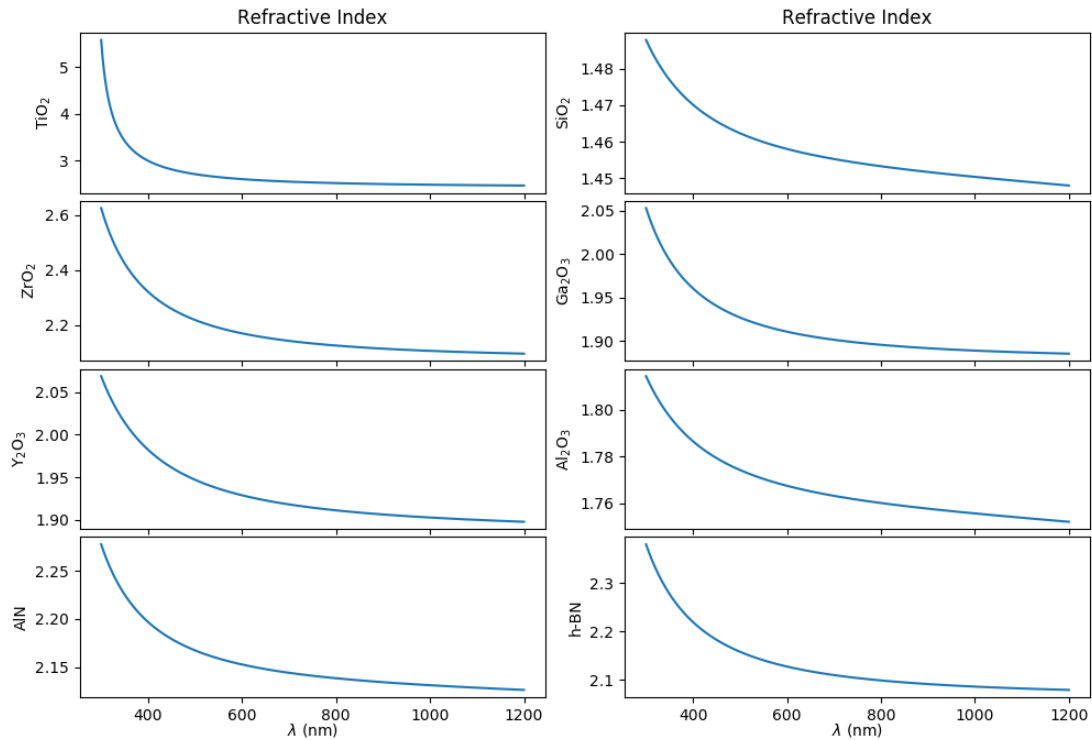


Figure 3.1 : Wavelength-dependent refractive index of chosen materials

While simulating optical behavior of thin film notch filters, we have been focused on the visible and infrared regions of the electromagnetic spectrum. Hence, the wavelength-dependent refractive index of chosen compounds has been plotted between 300 nm and 1200 nm according to their dispersion equations.

The library of the materials that is part of our simulation has been presented in Appendix A.1 section.

3.2 Single-layer Modeling

In the second part of the simulation, the single-layer model of a thin film structure has been performed. Every material in the database simulated with around 50 and 100 nm film thickness on the substrate. These single-layer models are significant both the calibration thickness monitoring part of the coating system and correction of the simulation. Since the thickness and optical property compatibility between numerical modeling and experiments are essential for this study.

Before modeling of multilayer stacks, transmission and reflection features of single-layer coatings have been simulated with the different film thickness in order to observe material dependency on the optical properties.

Besides, a chart of transmittance - reflection - wavelength - film thickness has been plotted to preview the film thickness and wavelength of the incident light effect of the formation of constructive interferences for each chosen material. Not only this chart but also transmittance and reflectance figures of the single-layer structures have been shown in Chapter 5.3.3.1.

Calculations about single-layer models of the simulation have been presented in Appendix A.2 section.

3.3 Multilayer Modeling

In order to obtain notch filter behavior using interference phenomena of electromagnetic waves, it is necessary to create a multilayer thin film structure from at least two different materials. Furthermore, the characteristic matrix of each thin film is needed for calculating the optical properties of multilayer structures. The number of repeated layer pair affects the optical properties of the multilayer stack.

The characteristic matrix of the multilayer thin film filter is given below in terms of the characteristic matrix of two chosen materials which are i and j , representatively.

$$M_{ij} = \underbrace{(M_i M_j)(M_i M_j) \dots (M_i M_j)}_{N\text{-times}} = (M_i M_j)^N \quad (3.1)$$

Where M_{ij} is the characteristic matrix of the multilayer filter, N number of the periodic thin film pairs, M_i and M_j are the characteristic matrix of i and j , respectively. As seen in Equation (3.1), the number of periodic film layers affects as a power of the characteristic matrix of the whole filter structure.

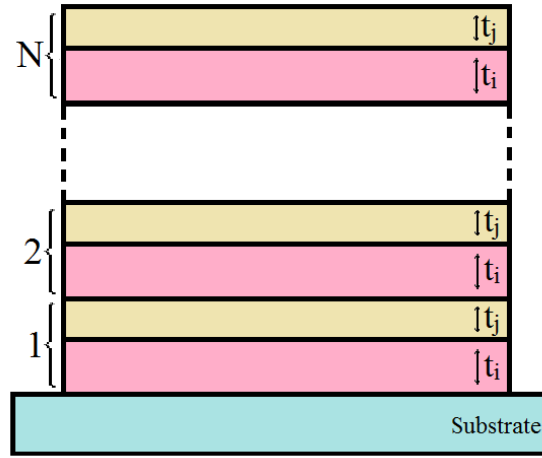


Figure 3.2 : Multilayer stack.

Figure 3.2 shows schematically the stack of thin film pairs on the substrate. Selected materials which are i and j in the figure, are simulated N -times periodically on top of each other with their specific thicknesses where t_i and t_j .

Notch filter behavior has been achieved by combining Equations (2.35), (2.41), and (2.42) in the second part with Equation (3.1). Several thin film notch filters have been simulated using different materials combinations and their different thickness variations.

Optical property results of simulated multilayer thin film notch filters have been given in Chapter 5.3.3.2.

The Python code about multilayer thin film notch filter simulation has been presented in Appendix A.3 section. In the calculations, a β parameter has been required for the correction of simulation with optical measurements. The definition and numerical value of this parameter will be stated in also Chapter 5.

4. THIN FILM FABRICATION TECHNIQUES

The thin film forming techniques can be basically classified as chemical vapor deposition (CVD) and physical vapor deposition (PVD). PVD techniques are dominant in interference filter fabrication technology. CVD is rarely used for multilayer optical filters [6].

4.1 Chemical Vapor Deposition

CVD is a kind of material deposition technique in which materials of a vapor phase and react with other gases or liquids to form solid material on a substrate. Reactant constituents are activated by different sorts of energy, so the CVD technique can be divided into subcategories according to an energy source such as thermal CVD (heat), photo-assisted CVD (radiation) or plasma-enhanced CVD (plasma). Furthermore, it is possible to classify CVD processes according to system design as hot-wall and cold-wall. While the whole chamber is heated up to reaction temperature in hot-wall CVD systems, the only substrate temperature is increased in cold-wall CVD applications. Except for these classifications, CVD methods can be categorized by operating pressure or type of precursor like; low-pressure CVD and metal-organic CVD.

Metals, nonmetallic elements, different types of compounds such as oxides, nitrides, carbides, alkyls, and many others can be deposited using the CVD technique. This technique is used for the synthesis of materials both thin film and powder form. If the reaction occurs in the homogeneous region of the chamber, product materials are powder form. For a thin film coating on a substrate, the reaction should occur in the heterogeneous part of the reaction chamber (Figure 4.1). Manufacturing thin films by CVD is significant for the electronic industry and wear-resistant coatings on tools. However, CVD is used less often for optical applications.

There are both advantages and drawbacks of the CVD technique when compared to PVD techniques. The most outstanding advantage of CVD is that it is not a

line-of-sight procedure, so the coating of three-dimensional objects and pipes is possible. Also, the CVD process does not require plasma generation except for the plasma-enhanced CVD method. Generally, CVD processes have a high deposition rate, so coated films are dense.

Unlike these advantages, CVD techniques have some disadvantages. The significant drawback is process gases and products of CVD are usually toxic and corrosive. This occasion threatens lives and the environment. Hazardous products need a neutralization process after manufacturing, but this additional process increases fabrication cost. Also, CVD processes require high process temperatures (around 1000 °C), and it is not suitable for some substrates that have low melting or glass transition temperature.

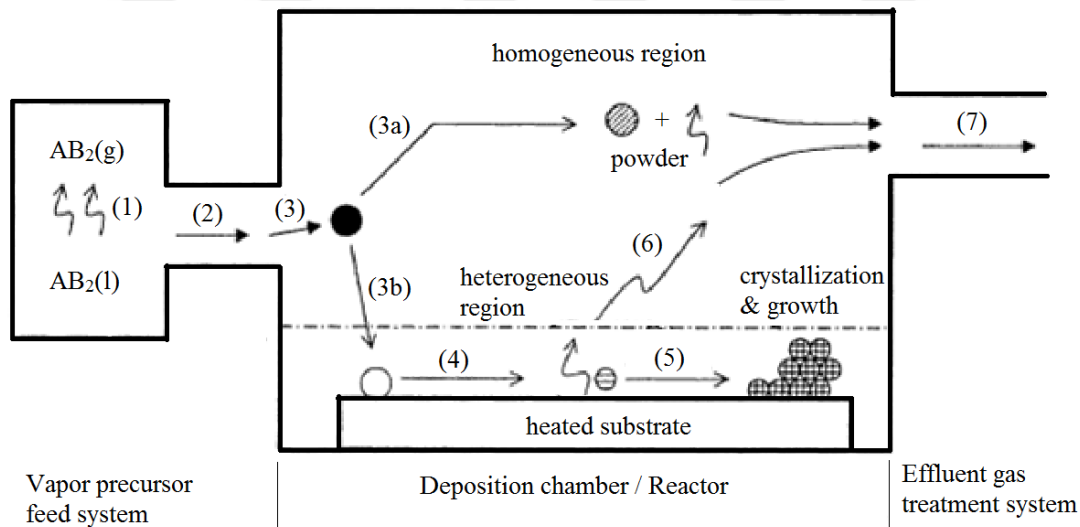


Figure 4.1 : Basic cold-wall CVD system and deposition mechanism [13].

Figure 4.1 introduces schematically a basic cold-wall CVD system and steps of deposition with a number from 1 to 7 [13]. In the first step, reactant gases are generated in the vapor precursor part of the system. Produced vapors transport into the deposition chamber (2). Then, the reaction among vapors occurs. The form of a product depends on the reaction region. (3a) and (3b) represent homogeneous and heterogeneous zones of the chamber.

After, vapor reactants are adsorbed on the heated substrate, and the heterogeneous reaction occurs at a gas-solid interface in the 4th step. Deposited materials diffuse along the heated substrate in (5). Also, film growth and crystallization are formed,

simultaneously. In (6) and (7), unreacted gases are removed from the film surface and reactor.

4.2 Physical Vapor Deposition

PVD is another technique to fabricate a thin film. PVD techniques utilize momentum and kinetic energy transfer or heat energy for vaporizing coating materials. Unlike the CVD process, source material should be a solid phase in the PVD methods. History of PVD is back to the 19th century, but it has become more common after the development in vacuum technologies in the last decades. PVD techniques need high vacuum conditions (generally $10^{-2} - 10^{-4}$ Pa). Vacuum rate has a crucial role in vaporizing source material because the mean free path of atoms or molecules increases under the high vacuum condition. The definition of the mean free path is the average distance of moving particle between two collisions. As the number of atom/molecule in the medium is decreased, the mean free path increases because unreacted particles behave like a barrier during the process. So, particles which are used for vaporizing source have more velocity through applied voltage. Besides, vacuuming reduces contamination risk.

Almost all types of materials can be coated by PVD. Deposition occurs by condensation in the PVD technique, and it does not include chemical reactions. The main disadvantage of PVD is that it line-of-sight process, so it is not appropriate for three-dimensional coating. On the other hand, PVD techniques do not require a high process temperature. Room temperature is enough for some applications. This property provides minimum distortion on the coated materials. PVD is an environmentally friendly process, so it does not require additional precautions. Materials that have a high melting point can be coated easily using PVD techniques.

Phase transition of coating material into the vapor phase can be completed in two methods in PVD: sputtering and evaporative.

4.2.1 Sputtering

Sputtering is one of main PVD method which is based on momentum transfer of atomic-size particles. In the sputtering process, source materials, named as a target, is bombarded by accelerated process gas. Surface atoms or molecules of the target

material are physically ejected through the momentum transfer of process gas. This technique needs high vacuum conditions for increasing the mean free path of particles for obtaining higher particle momentum. The atomic-size particles are accelerated by high voltage. Particles should be charged for acceleration, so cold-plasma is generated in the sputtering process. Ejected target atoms or molecules are deposited on the substrate by the applied bias voltage.

The sputtering technique is a non-thermal process, but it requires a plasma generation and a high vacuum environment. Sputtering PVD method is commonly used for the coating of refractory materials, semiconductor industry, reflective coatings, and jewelry industry.

Sputtering process can be divided into sub-categories according to the working principle of systems such as a diode, triode, magnetron, and ion-beam sputtering, but diode and magnetron sputtering techniques have been briefly explained in the present work.

4.2.1.1 Diode

The diode is the simplest sputtering method. After applying a high voltage to solid target and substrate, they become cathode and anode respectively. Between the cathode and anode (distance is approximately 5 - 15 cm) plasma is generated using process gas. Argon (Ar), a noble element, is chosen as a process gas in many coatings. During the plasma generation, Ar atoms are positively charged, and they accelerated toward cathode by high voltage. Accelerated atoms are bombarded with the target surface, and their momentum is transferred to target surface atoms. This process is illustrated in Figure 4.2 [26].

Finally, ejected target particles moved to the anode and, they are deposited on the substrate.

In the diode technique, both target and substrate should be solid and conductive. The main drawback of this process is the low ionization rate ($\sim 10\%$).

The low ionization rate of Ar atoms decreases the sputtering yield and accordingly deposition rate.

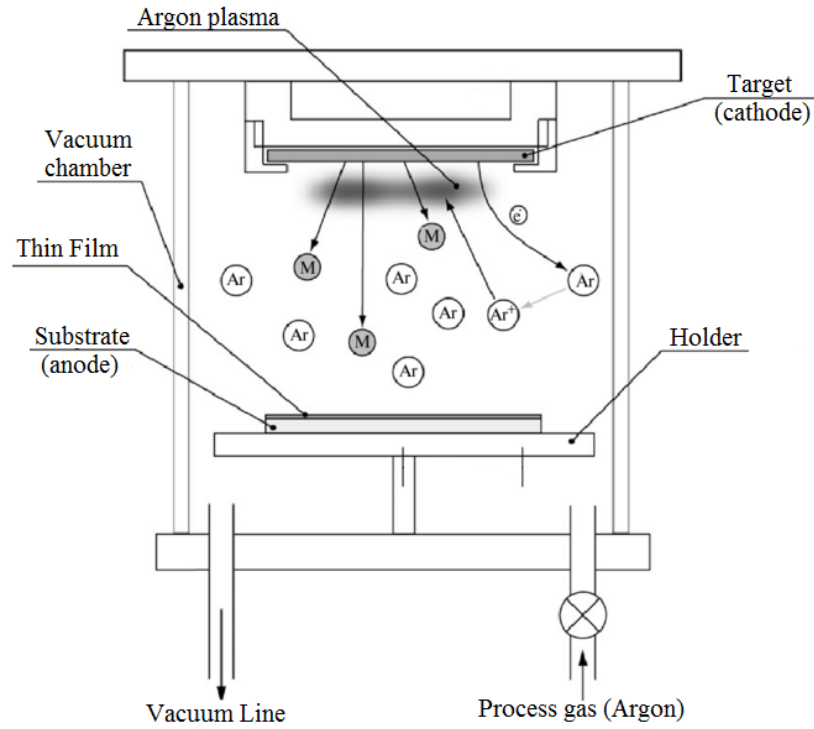


Figure 4.2 : Schema of the diode sputtering technique [26].

4.2.1.2 Magnetron

Magnetron sputtering is a modified form of diode process. In addition to the diode, magnets are placed bottom of a target in the magnetron sputtering method (Figure 4.3 [27]).

The magnet system helps to attract and accelerate Ar atoms to target. More Ar ions can reach to target; consequently, sputtering yield increases. Sputtering yield can be expressed in Equation (4.1).

$$\text{Sputtering yield } (S) = \frac{\text{Number of the ejected particles}}{\text{Number of the incident ions}} \quad (4.1)$$

S depends on the mass and energy of the process gas. As mass and speed of incoming ions increases, sputtering yield approaches to 1. Also, S is affected by the mass and binding energy of target atoms. Increasing mass and binding energy of target atoms decrease sputtering yield.

Geometry is the third parameter. 60 - 70 degrees is the most efficient incident angle for achieving a high sputtering yield.

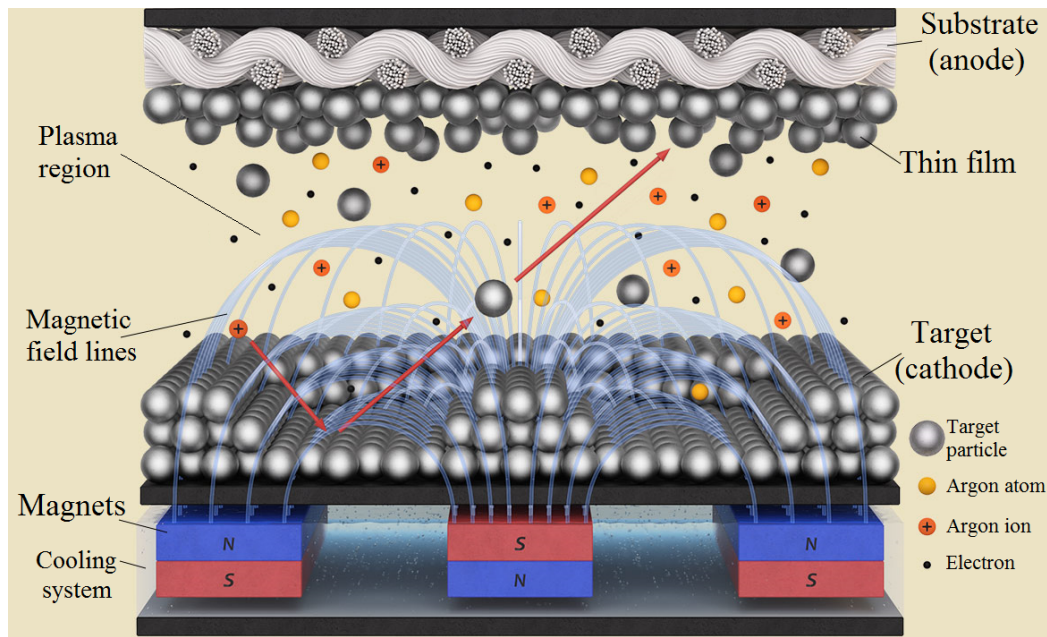


Figure 4.3 : Illustration of the magnetron sputtering process [27].

As sputtering yield increases, the deposition rate increases. One of the main disadvantages of the sputtering method can be eliminated through magnets. In the magnetron process, the substrate temperature is relatively lower than the diode method. Magnetron technique is quite suitable for industrial-scale applications.

4.2.2 Evaporative

Another type of PVD technique is the evaporation process. The evaporative coating procedure is based on the melting or directly sublimating of the source materials. After transition source material to the gas phase, vaporized particles are condensed on the substrate in a high vacuum condition. Unlike sputtering, evaporative PVD process requires neither plasma nor process gas. The distance between the source material and substrate is longer than the sputtering process because of avoiding substrate heating. The major disadvantage of evaporative PVD is non-uniformity in film thickness. The radial flux of coating materials causes thickness differences between the center and edges of the substrate. Rotating (planetary) substrate holder can be effective while obtaining more homogenous coating in terms of thickness. Coating thickness is measured by the thickness monitoring system which is placed near the substrate.

Evaporative PVD technique is classified according to evaporation sources as resistive, inductive, electron beam, cathodic arc, and laser ablation, but resistive and electron beam methods have been briefly explained here.

4.2.2.1 Resistive

The resistive evaporation method is the most primitive one among the evaporative PVD techniques. Source materials are evaporated or sublimated by a resistively heated source. Electric current flows across the heating resistance material (generally Mo, Ta, and W) and the source material in the crucible is melted or sublimated. The selection of resistance materials depends on the source material [28].

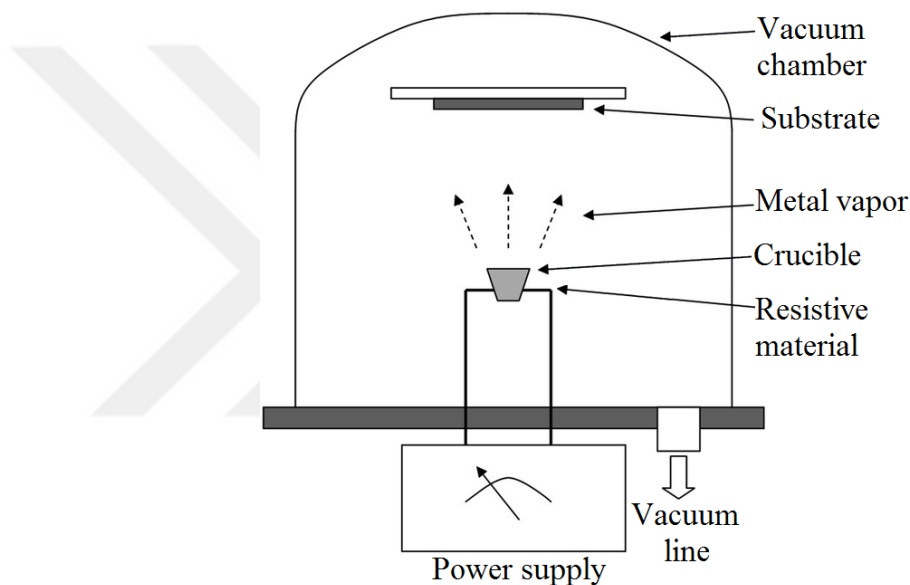


Figure 4.4 : Resistive evaporation method [28].

Resistive evaporation systems can be used for only materials that have a low melting point. It is not a good way to coat refractory materials. Some chemical reactions can occur between source material and crucible, and this may cause contamination.

4.2.2.2 Electron Beam

In the electron beam (E-beam) evaporation technique, the source material is vaporized by the kinetic energy transfer of electrons. Source material can be heated up to several thousand Celsius through of electron beam. Consequently, even refractory materials can be coated using this method.

Typically, electrons are emitted from cathodic tungsten filament by the applied alternative current. Alternative current is preferred because it is hard to reach high

temperatures on crucible using direct current. The filament is hidden under the crucible for avoiding contamination. The schematic representation of the E-beam evaporation system is given in Figure 4.5.

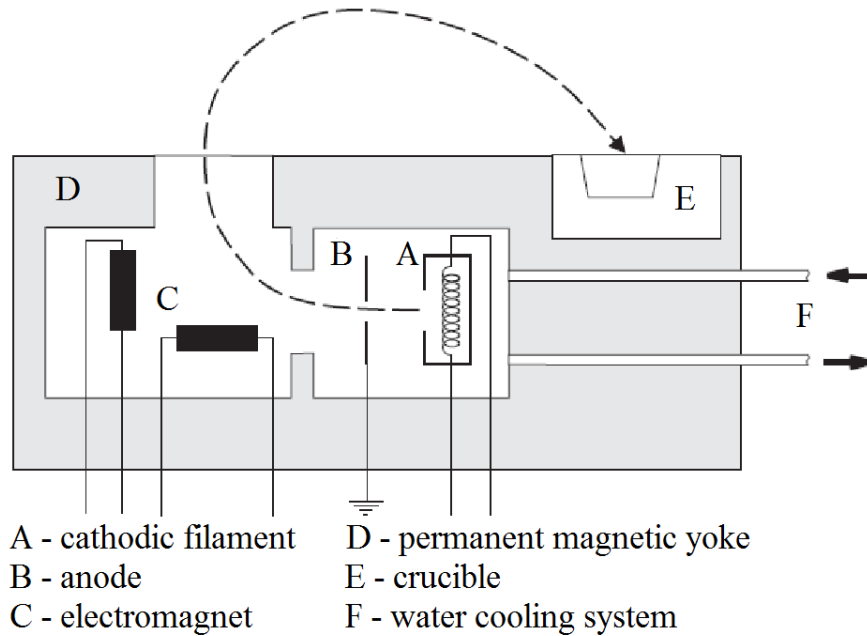


Figure 4.5 : Electron beam evaporation technique [2].

It is shown in Figure 4.5 that emitted electrons pass from the small hole on the anode; thus, a homogeneous electron beam with a tiny diameter is obtained. The created electron beam is deflected on the coating material through magnets after their radial movement. Free electrons are focused on the source material by applied high voltage (5 – 10 kV). The position of the electron beam is tuned by magnet current (0 – 3 A DC) and potential (-2 to +2 V DC). The intensity of the electron beam is controlled by emission current (0 – 1 A DC). When the coating material starts to evaporate, it deposits on the substrate. There is a water-cooled system below the crucible, so walls of the crucible remain cold. This system decreases the contamination risk.

Crucible holder can rotate, and 4 – 6 crucibles can be placed on it. This feature is crucial for multilayer coating using different source materials. Moreover, the substrate holder also can rotate so the production of spiral and oblique coatings is possible. A high vacuum which is around 10^{-4} Pa is essential for the E-beam evaporation process. The E-beam evaporation is a universal technique for optical coating, but the system is expensive.

In the present study, we decided to use the E-beam evaporation technique during thin film coating procedures.





5. EXPERIMENTAL PROCEDURES

5.1 Thin Film Coating System

As mentioned in previous sections, the thin film deposition process has been completed using the E-beam evaporation technique. Our coating system is composed of five main parts which are; the vacuum chamber, the vacuum control unit, the E-beam control unit, the thickness monitoring system, and the water cooling system. The parts of the coating system are shown in Figure 5.1.

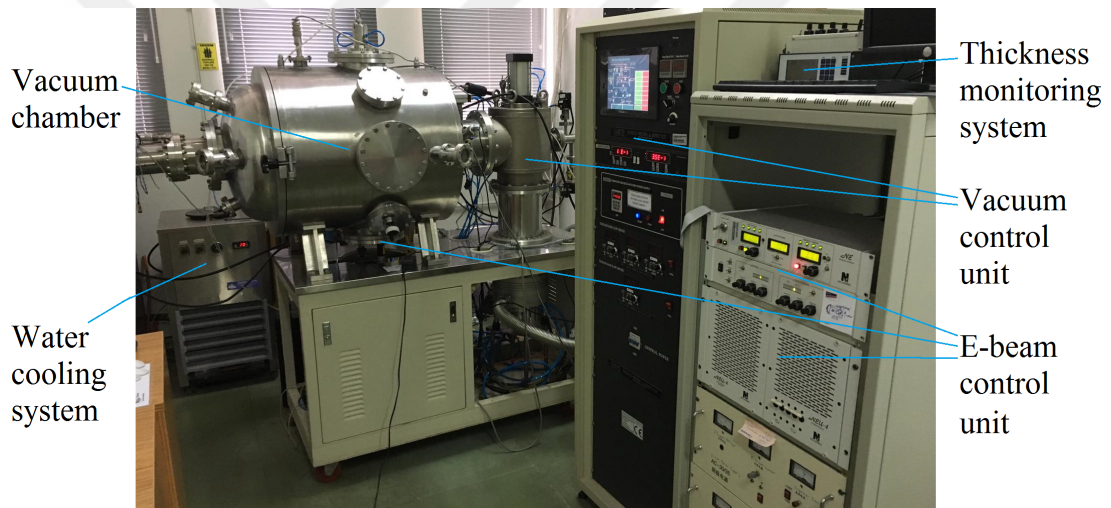


Figure 5.1 : The coating system.

5.1.1 The vacuum chamber

The thin film deposition procedure has been completed in a cylindrical vacuum chamber. The chamber was made of stainless steel, and its dimensions are 64 cm diameter and 67.5 cm length. The E-beam evaporation source is located in the mid-bottom of the chamber. Six crucibles, 4 cc of each, can be placed at the same time in the rotatable crucible holder mechanism. The water cooling system prevents crucibles from excessive heating. The distance between the crucible and the substrate is 16 cm.

5.1.2 The vacuum control unit

Vacuuming such a big chamber requires powerful vacuum pumps. As a mentioned previous chapter, a high vacuum level is essential for obtaining good quality coating. The vacuum control unit is consists of two main components which are a rough vacuum and high vacuum parts. Before reaching high vacuum levels (between 10^{-3} and 10^{-6} Pa), the chamber should be in a rough vacuum level (around 10^0 Pa). So, the pressure is decreased to a rough vacuum level by a mechanical pump, and then the system is reached to a high vacuum level by a molecular pump in the operation chamber. Total pumping duration takes approximately 3 - 4 hours due to the big volume of the chamber. The thin film coating processes have been started around 9×10^{-3} Pa vacuum environment.

5.1.3 The E-beam control unit

After reaching the desired high vacuum level, the E-beam control unit became ready for activation. The E-beam evaporation source is presented in Figure 4.5 Alternative current has been applied to tungsten filament for ejecting free electrons. In the whole experimental procedures, free electrons have been oriented to coating material by 6.00 kV high voltage. E-beam has been deflected and focused on the middle of source material by tunable electromagnets. In order to start evaporation in the vacuum chamber, the emission current has been slightly increased. The magnitude of the emission current depends on the coating materials.

The evaporation rate of the materials differs according to sublimation capability, mass, chemical purity features. The vacuum level also affects the emission current due to a change in the mean free path.

5.1.4 Thickness monitoring system

As mentioned, each film thickness has a crucial role in achieving high-quality optical properties, so accurate control of the deposition rate is necessary. During the coating process, the deposition rate, coating thickness, and duration can be determined by the thin film deposition controller. The brand-model of our thickness monitoring device is

Inficon-XTC/2. In the operation chamber, there is a measuring head which is located near the substrate holder. It is kept at a constant temperature through the water cooling system for avoiding temperature-dependent measurement mistakes in thickness. The measuring head consists of a quartz crystal measurement system which oscillates at high frequency (~ 5.6 MHz). Quartz crystal is made of gold. The measurement of film thickness depends on the simultaneous oscillation frequency and mass density of the coating materials. The principle is that quartz crystal is also coated with the source material, and the oscillation frequency decreases while the material is depositing on it. The mass of deposited materials is calculated using frequency decreasing. Since the area of quartz crystal, z-ratio, and material density are known, the deposition rate can be calculated, simultaneously. The integration of the deposition rate to process duration gives the total thickness of the film. All calculated and measured parameters are monitored on the screen.

5.2 Selection of Coating Materials

Chosen materials for simulation have been given in Figure 3.1. Three of them have been selected for deposition studies. Chemical and physical characteristics of materials have been decisive in material selection. The accessibility of materials was another important subject.

Chemical purity, refractive index, mass density, transparency range, the suitability of the E-beam evaporation technique have been considered while deciding coating materials. Finally, Al_2O_3 , Y_2O_3 , and SiO_2 have been chosen for multilayer thin film notch filter fabrication procedures. A refractive index gap among three dielectric materials has been provided transmittance bands when they coated as periodic multilayer stack.

5.2.1 Al_2O_3

The first selected material is Al_2O_3 , and it has been obtained in powder form with 99.99% chemical purity. Nevertheless, coating material should be in bulk or granulate form for the E-beam evaporation technique because it is a possible scattering of powders after electron beams collide them. Spread powders can cause defects on a substrate and contamination in the chamber.

Therefore, Al_2O_3 powders were pressed in small latex packs by the cold isostatic pressing (CIP). The amount of pressure was equal to 624.52 MPa on each package surface. After the CIP process, bulk Al_2O_3 formed in a spherical shape. Heat treatment applied to the final form of material for 1 hour at 800 °C for eliminating polymeric impurities.

Suitability of Al_2O_3 is excellent for the E-beam process and it directly sublimates when it is exposed to the electron beam. The general features of Al_2O_3 are given in Table 5.1 [29].

Table 5.1 : The general features of Al_2O_3 [29].

Coating material	Film composition	Mass density (g/cm ³)	Transparency range (nm)	Refractive index (at 500 nm)	z-ratio
Al_2O_3	Al_2O_3	3.970	0 - 1000	1.7742	0.336

5.2.2 Y_2O_3

The second chosen material is Y_2O_3 . Likewise Al_2O_3 , Y_2O_3 has been available as powder form in the laboratory with 99.99% purity. Y_2O_3 powders were filled in the same elastic packs, and the CIP process applied to them. Bulk Y_2O_3 was obtained under 451.04 MPa in a smooth spherical shape. Before placing in the graphite crucible, spherical Y_2O_3 samples also stayed 1 hour at 800 °C.

Y_2O_3 can be coated easily by the E-beam evaporation technique. The properties of Y_2O_3 are shown in Table 5.2 [30].

Table 5.2 : The general features of Y_2O_3 [30].

Coating material	Film composition	Mass density (g/cm ³)	Transparency range (nm)	Refractive index (at 500 nm)	z-ratio
Y_2O_3	Y_2O_3	5.010	0 - 8000	1.9474	1.000

5.2.3 SiO_2

The last preferred material for the coating procedure is SiO_2 . It has been obtained as a nano-powder form with higher than 99.99% chemical purity. Similar to Al_2O_3 and Y_2O_3 powders, SiO_2 white nano-powders were filled in small packages, and then they

were pressed by the CIP. The pressure was equal to 624.52 MPa on packets. At the end of the CIP process, tiny SiO₂ transparent samples were formed. For removing residual polymer particles, formed SiO₂ bulks were exposed to the heat-treatment. Suitability of SiO₂ is excellent for the E-beam method, and it can be coated by direct sublimating. The characteristics of SiO₂ are presented in Table 5.3 [31].

Table 5.3 : The general features of SiO₂ [31].

Coating material	Film composition	Mass density (g/cm ³)	Transparency range (nm)	Refractive index (at 500 nm)	z-ratio
SiO ₂	SiO ₂	2.648	0 - 9000	1.4623	1.000

5.3 Experiments, Analysis, and Results

Both simulated and fabricated thin film structures will be presented and analyzed with their surface and optical characteristics. As mentioned in previous sections, before manufacturing multilayer thin film notch filters, single-layer coatings of three chosen materials have been produced with two different film thicknesses. Since our thickness monitoring system needed a calibration. Besides, the simulation needed a correction for better optical accuracy with measured data of fabricated samples. Surface analysis was done by Nanomagnetics/ezAFM atomic force microscopy (AFM). KLA Tencor/P-7 surface profiler was used for thickness measurements of single-layer coatings. Optical properties of both multilayer stacks but also single-layer structures were measured by Shimadzu/UV-3600 spectrophotometer.

5.3.1 Surface analysis

Optical behaviors are highly affected by the surface features of thin film and substrate. Impurities, defects, and surface roughness negatively affect transmittance and reflectance. Incident light is more likely to scatter from a high amount of impurities, defects, and surface roughness. Corning®-2947 glass slides have been preferred as a substrate because Corning®-2947 micro slides are used for special optical applications and using them is a good way to reduce defect risk on the substrate.

The dimension of one slide is 75 mm × 25 mm, but it was divided into two before coating. So, the dimension of one coating sample equals 37.5 mm × 25 mm.

For vanishing impurities on the surface, substrates were cleaned with acetone, ethyl alcohol, and pure water in the ultrasonic cleaner, respectively.

The surface roughness of thin film depends on the coating material type, the deposition rate and the thickness of the layer. Therefore, deciding the optimum deposition rate for next coatings, several single-layer coatings have been produced with different deposition rate and film thickness for each material.

The measure of surface roughness is the average R_a value, with nm unit. R_a value of single-layer coatings was measured by AFM. 3D surface topography of single layer coatings are given in Figure 5.2 - 5.4 . Table 5.4 shows the surface roughness of single-layer samples which were produced according to various parameters. 3D surface topography images of single-layer coatings are presented in the following figures.

Table 5.4 : Surface roughness of single-layer coatings.

Film material	Film thickness (nm)	Deposition rate ($\text{\AA}/\text{s}$)	Average R_a (nm)
Al_2O_3	136	4.0	2.98
Al_2O_3	71	4.0	1.23
Al_2O_3	69	8.0	1.22
Y_2O_3	130	4.0	1.77
Y_2O_3	79	4.0	0.60
Y_2O_3	73	8.0	1.02
SiO_2	128	5.0	1.05
SiO_2	66	5.0	0.72

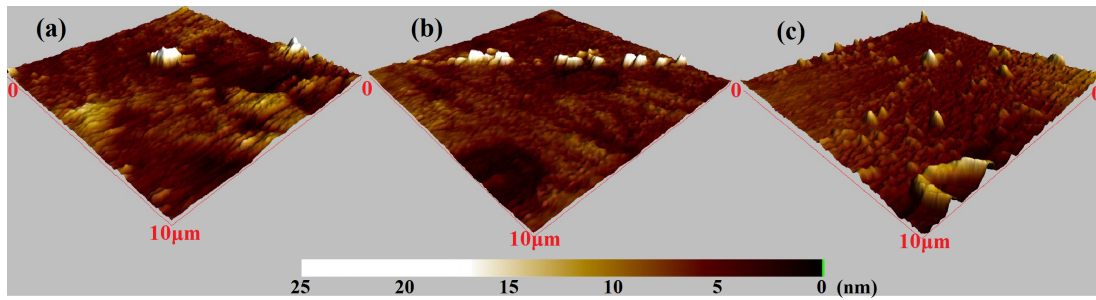


Figure 5.2 : 3D topography of single-layer Al_2O_3 coatings with average R_a = (a) 2.98 nm, (b) 1.23 nm, and (c) 1.22 nm.

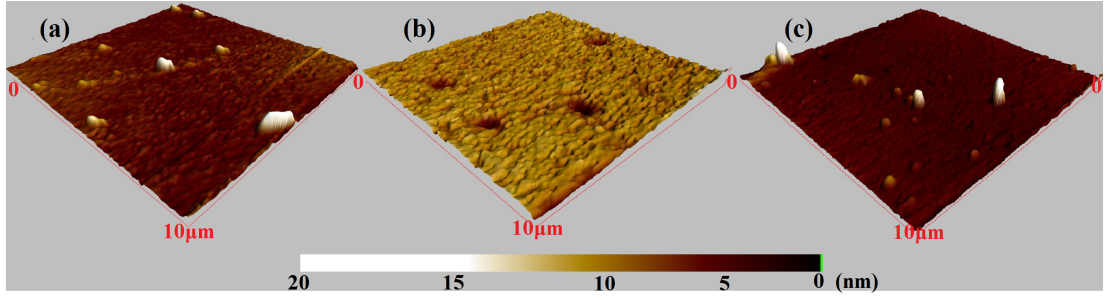


Figure 5.3 : 3D topography of single-layer Y_2O_3 coatings with average R_a = (a) 1.77 nm, (b) 0.60 nm, and (c) 1.02 nm.

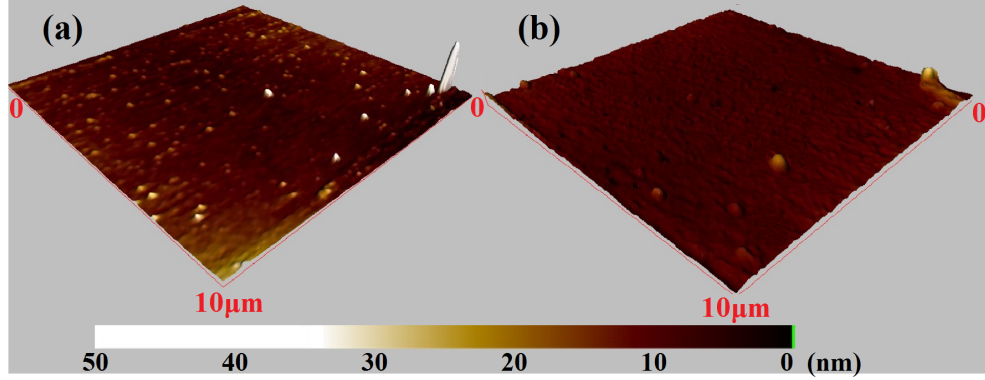


Figure 5.4 : 3D topography of single-layer SiO_2 coatings with average R_a = (a) 1.05 nm, and (b) 0.72 nm.

According to literature, as the mass density of coating material increases, the surface roughness of the thin film increases. However, we could not observe this effect despite the density difference between Al_2O_3 and Y_2O_3 coatings. Table 5.4 states that average R_a value increases while layer thickness is increased in all material types. It is hard to form a smooth surface when the number of deposited particles is in large quantities. This surface roughness–thickness relation is supported by a study of Leng and his collaborators. In order to obtain a smooth surface, meanly low surface roughness, the diffusion rate of adatoms on the substrate should be higher than the flux of evaporated particles. Consequently, high depositions rate cause roughness on the film surface [32] [33].

As a result of AFM analysis, we have been decided to fabricate multilayer thin film notch filters with a 4.0 - 5.0 Å/s deposition rate to achieve low surface roughness as much as possible.

5.3.2 Thickness measurement

In order to fabricate aimed thin film notch filters, the thickness calibration of the thickness monitoring system according to the real thickness of layers is essential. So,

before the production of multilayer structures, the thickness monitoring part of the E-beam system has been calibrated using single-layer coatings. Film thicknesses of single-layer samples were measured by the surface profiler and they were compared to that measured by the thickness monitoring system. The comparison of two data-set is given in Table 5.5.

Table 5.5 : Measured film thickness comparison by the thickness monitoring system and surface profiler.

Film material	Film thickness (nm)	
	Thickness monitoring system	Surface profiler
Al ₂ O ₃	120	136
	60	71
	60	69
Y ₂ O ₃	120	130
	60	79
	60	73
SiO ₂	120	128
	60	66

The disagreement between the two measurement methods mostly arises from the difference between the theoretical bulk mass density input of the thickness monitoring system and the film density of the coating material. The small variations between mass density values can cause big thickness deviations after the complex calculations that the thickness monitoring system done. Equation (5.1) is quite useful to minimize such thickness deviations. The mass density of each coating material can be adjusted using its theoretical density, real and deviated thickness values.

$$\rho_{ad} = \rho_{th} \left(\frac{t_x}{t_m} \right) \quad (5.1)$$

where ρ_{ad} is adjusted and ρ_{th} is theoretical mass densities of the coating material. t_x and t_m are the thicknesses that reading on the display and measured by surface profiler, respectively. Equation (5.1) belongs to the operating manual of Inficon-XTTC/2. After this density modification, thickness disagreement declines below 10%. The average adjusted mass densities of selected coating materials are given in Table 5.6.

Table 5.6 : Adjusted mass density of the coating materials.

Film material	Mass density (g/cm ³)	
	Adjusted (average)	Theoretical
Al ₂ O ₃	3.437	3.970
Y ₂ O ₃	4.183	5.010
SiO ₂	2.445	2.648

The compatibility of simulation and experiments in terms of thickness is also essential. The harmony of simulation and experiment results is investigated through characterizations of optical behaviors.

5.3.3 Optical Behaviors

5.3.3.1 Single-layer

Simulation

Before simulating multilayer structures, single-layer thin films have been simulated in order to comprehend the general optical behavior of each material in the materials database.

Thereof all materials have been simulated with different film thickness and they have been plotted in the same graph to see their optical behavior in Figure 5.5 and Figure 5.6.

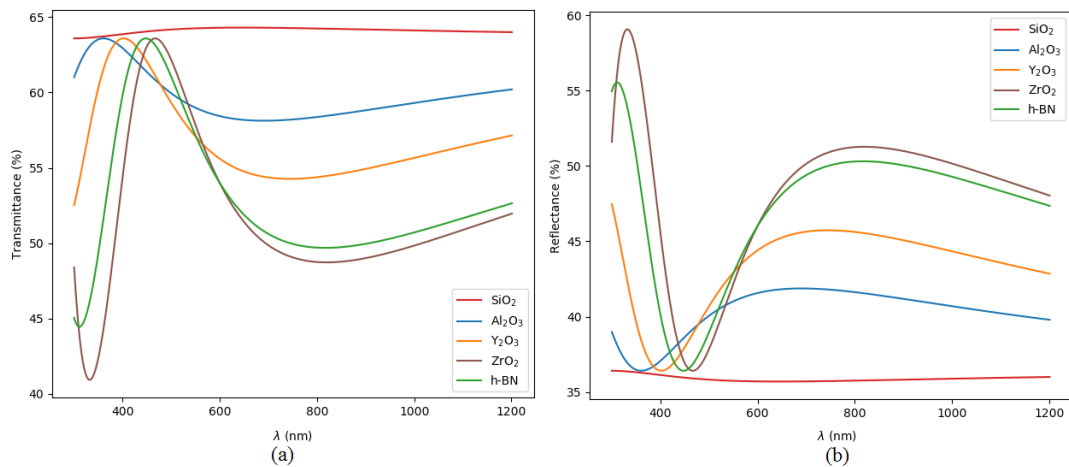


Figure 5.5 : Transmittance (a) and reflectance (b) of 100 nm single-layer modeling for different materials.

Figures 5.5 and 5.6 have been generated according to the characteristic matrices of materials and Equations (2.41)-(2.45). As shown in previous figures, coating materials have unique behavior in terms of transmittance. It can be understood that the thickness of the layer controls the transmittance curve when comparing Figure 5.5 (a) and Figure 5.6 (a).

In single-layer modelling, absorption has been neglected, so the sum of T and R is equal to 1.

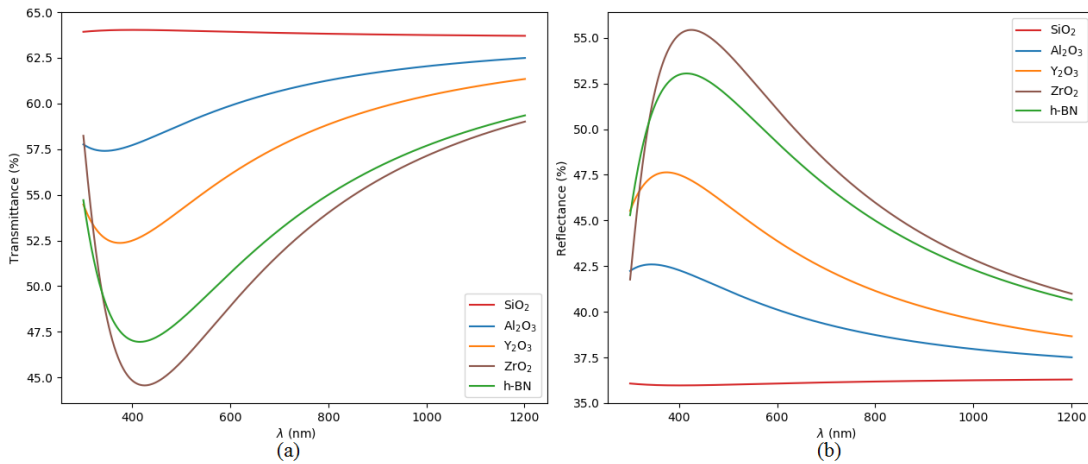


Figure 5.6 : Transmittance (a) and reflectance (b) of 50 nm single-layer modeling for different materials.

Figure 5.7 basically indicates constructive and destructive interferences. The high amount of transmitted and reflected light is represented by bright lines on top of the figure. There is a correlation between film thickness and wavelength for destructive interference.

Generally, destructive interference occurs when the minimum film thickness equals one-quarter of wavelength for non-reflective structures. Figure 5.7 is useful to visualize both constructive and destructive interferences as a function of film thickness and wavelength.

Thus, material combinations can be determined for multilayer designs using this relation.

Figures 5.5, 5.6, and 5.7 do not include TiO_2 , Ga_2O_3 , and AlN due to avoid complexity in figures. But, they can be taken into account easily if required.

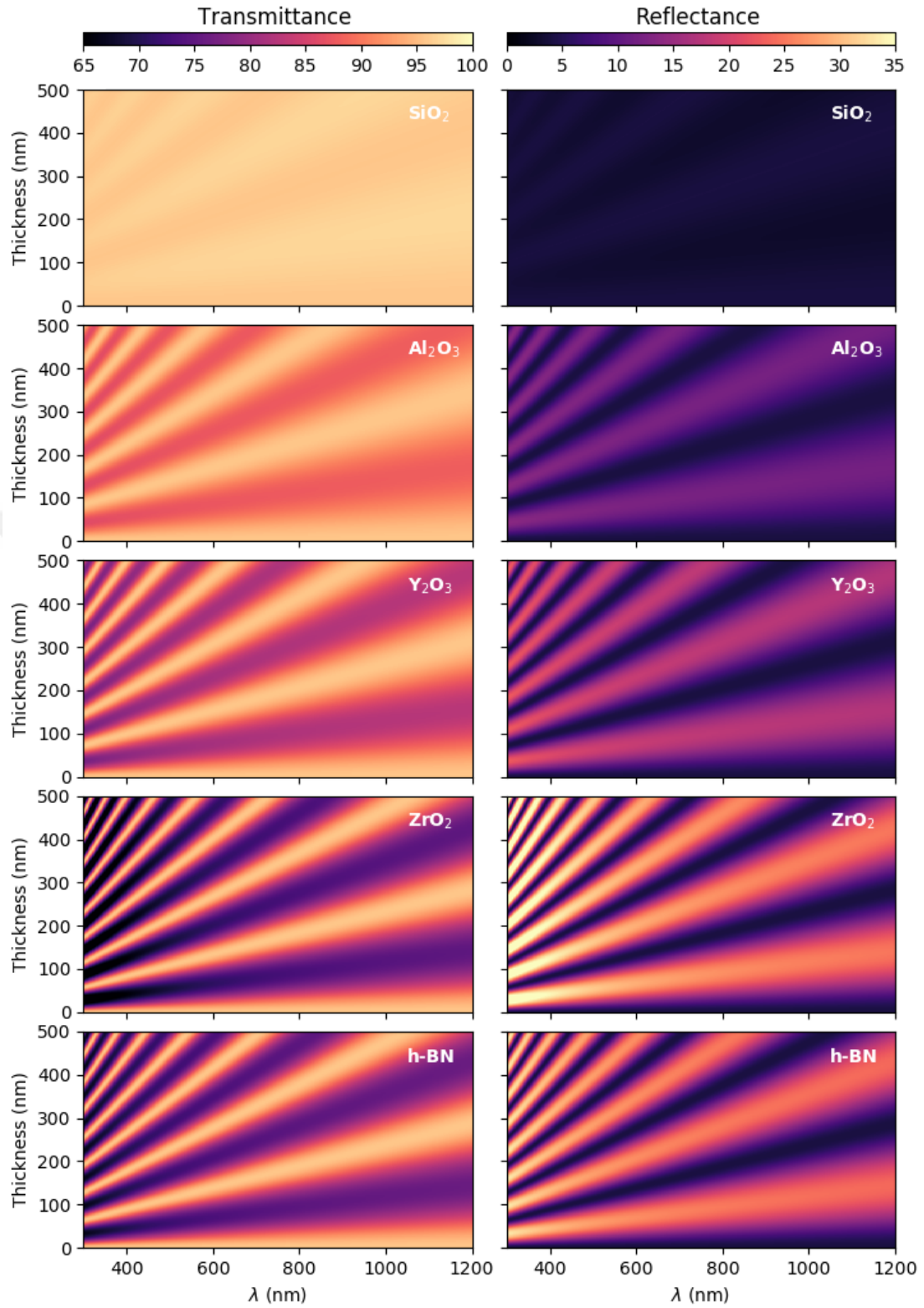


Figure 5.7 : Thickness - wavelength - transmittance - reflectance relation of various single-layer thin film materials.

Fabrication

The optical characterization of fabricated single-layer coatings gives information about the consistency of simulation. Since film thickness affects the optical features,

it is possible to predict the film thickness using reliable simulation. In order to test the reliability of our simulation, wavelength-dependent transmissions of single-layer coatings have been measured using the spectrophotometer and compared with simulated single-layer structures. Transmittance-wavelength graphs for each material are presented in the following figures.

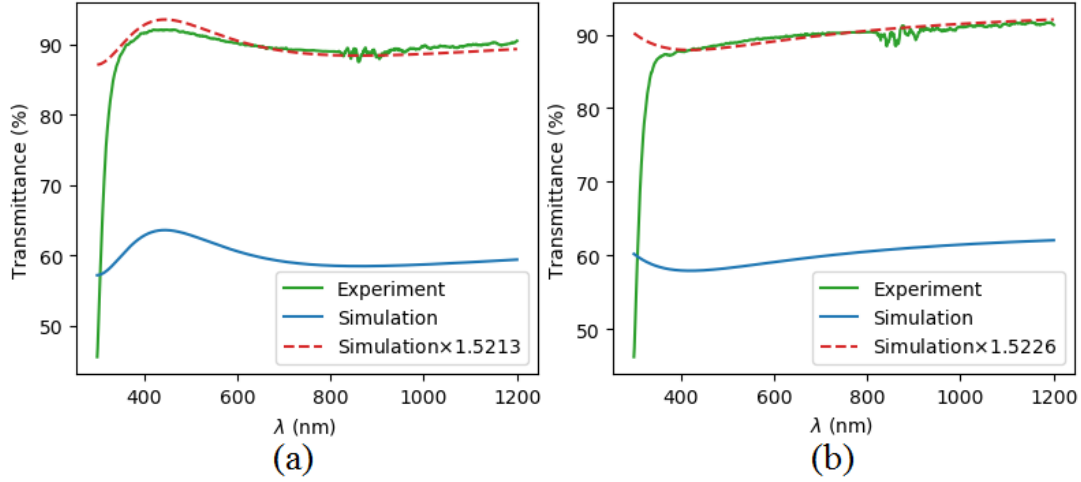


Figure 5.8 : Measured and simulated transmission values of (a) 136 nm, and (b) 69 nm Al_2O_3 films.

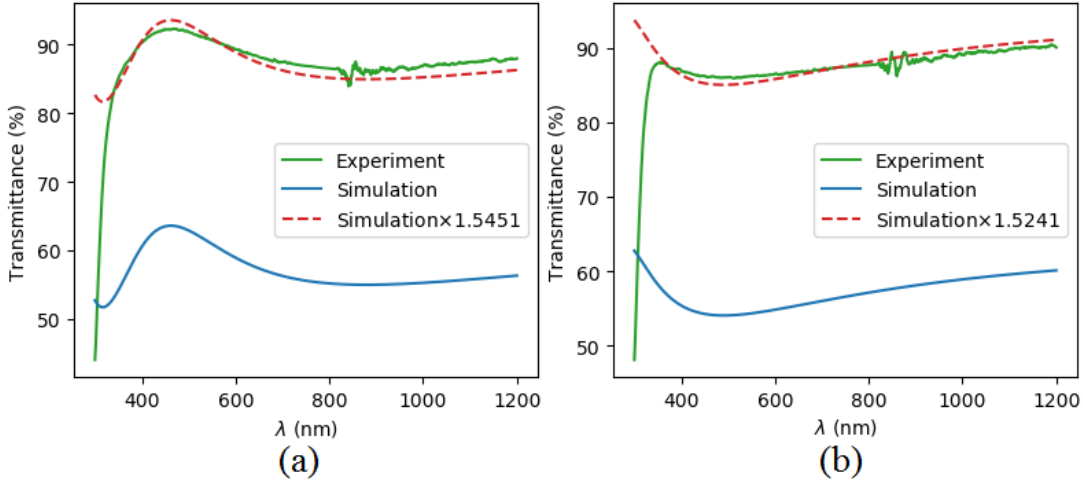


Figure 5.9 : Measured and simulated transmission values of (a) 130 nm, and (b) 73 nm Y_2O_3 films.

It has been appeared in all figures above that the magnitude of the simulation data requires multiplication with a parameter for better matching with measured data. This parameter equals approximately 1.52, and it will be called as β from now. It depends on neither film thickness nor type of film material.

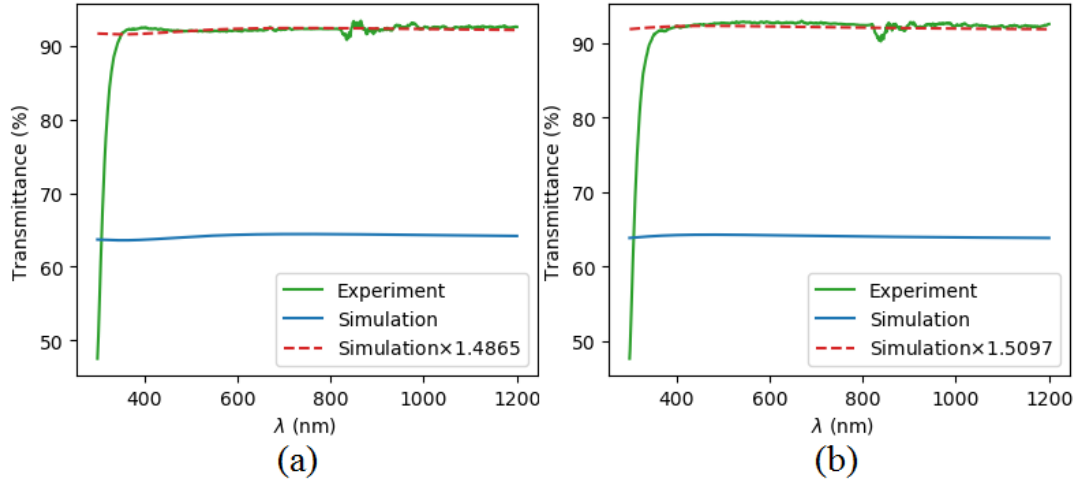


Figure 5.10 : Measured and simulated transmission values of (a) 120 nm, and (b) 69 nm SiO₂ films.

After the comprehensive literature survey, the constant has been revealed as the dimensionless normalization constant for simulation; moreover, it is equal to the refractive index ratio of substrate and air. Actually, this parameter comes up using the θ_t angle in the numerical model instead of the θ_i .

As a result, Equation (2.43) has been multiplied with β parameter and Equation (5.3) is obtained below.

$$\beta = \frac{n_s}{n_0} \quad (5.2)$$

$$T = \beta |t|^2 \quad (5.3)$$

In the next transmittance calculations Equation (5.2) has been used. There is a difference between the measured film thickness by the surface profiler and the thickness that the simulation predicted.

The expected thickness by simulation and measured real thickness is given in Table 5.7.

The absolute deviation between the expected and measured thicknesses is less than 10% that is acceptable for experimental studies. The thickness difference may arise for two reasons. The first reason may be the sensitivity of the measuring device. The

Table 5.7 : Comparison of expected and measured film thickness.

Film material	Film thickness (nm)	
	Predicted	Measured
Al ₂ O ₃	125	136
	62	69
Y ₂ O ₃	118	130
	67	73
SiO ₂	120	128
	66	69

error percentage due to measurement is around 1-2%. The second one may be minor variation in the Sellmeier dispersion equation of the film material.

Table 5.8 gives the deviation analysis results of single-layer coatings in terms of film thickness for each film material.

Table 5.8 : Absolute thickness deviation ratio of simulation and measurement.

Film material	Average absolute deviation (%)		
	Simulation	Measurement	Total
Al ₂ O ₃	7-8	1-2	9.12
Y ₂ O ₃	6-7	1-2	8.73
SiO ₂	3-4	1-2	5.30

5.3.3.2 Multilayer

Simulation

After the thickness calibration and correction of the simulation through the analysis of single-layer coatings, the coating system and simulation have been ready for the experiment on multilayer thin film structures.

Before the fabrication of multilayer thin film stacks, they have been simulated with various material combinations. Simulated multilayer thin film notch filters have been included not only chosen material combinations for fabrication but also other material combinations in the materials database of the simulation.

Some of simulated multilayer notch filters are presented in the following figures (Figure 5.11 - 5.14).

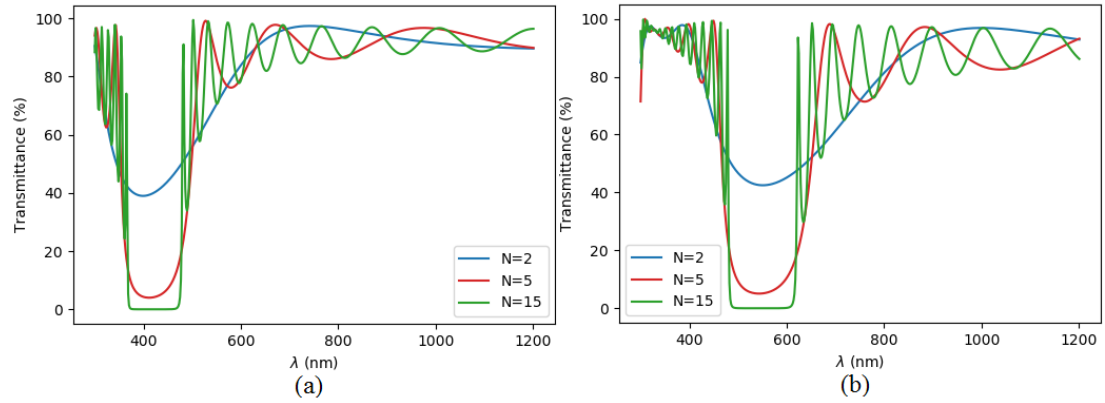


Figure 5.11 : Multilayer modeling of SiO_2 - h-BN combination.

In figure 5.11, the transmission of SiO_2 and h-BN film stacks are presented with different film thicknesses. Thickness of materials in Figure 5.11 (a) is $t_{\text{SiO}_2} = 40$ nm, $t_{\text{h-BN}} = 40$ nm. Thus, notch filter behavior has been achieved between 370 and 460 nm in the spectrum. This band encompasses the border of ultraviolet and visible regions.

When the thickness of SiO_2 layers was kept constant and the thin film thickness of the h-BN was increased to 70 nm, the filtering band has been shifted to 485 - 600 nm on the spectrum (Figure 5.11 (b)). This band corresponds to green and yellow colors. 30 nm difference in each layer of h-BN has been caused approximately 127 nm left movement on the spectrum line.

Also, this changing has been increased the notch filter bandwidth between (a) and (b) by 23 nm at full-width at half maximum (FWHM).

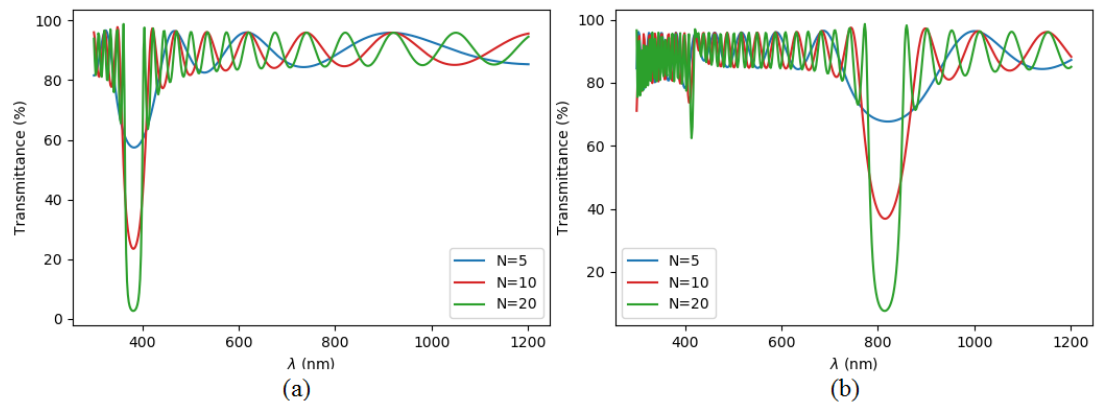


Figure 5.12 : Multilayer modeling of Al_2O_3 - Y_2O_3 combination.

Figure 5.12 shows two notch filter characteristics which are composed of Al_2O_3 and Y_2O_3 . (a) part of the figure has been obtained by $t_{\text{Al}_2\text{O}_3} = 50$ nm and $t_{\text{Y}_2\text{O}_3} = 50$ nm thin film pairs, respectively, and the center of notch filter has been located on 380 nm wavelength. The width of the band equals to 25 nm at FWHM.

When the film thickness of both materials has been increased from 50 nm to 110 nm, the near-infrared notch filter has been obtained. According to Figure 5.12 (b), the center of the near-infrared notch filter is around 800 nm and its bandwidth is 52 nm at FWHM.

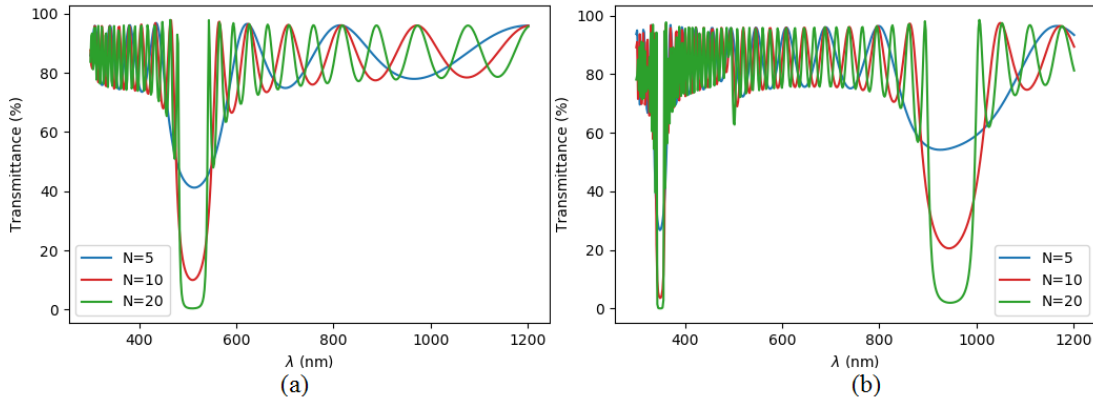


Figure 5.13 : Multilayer modeling of Ga_2O_3 - ZrO_2 combination.

For achieving monochromatic thin film notch filter, Ga_2O_3 and ZrO_2 can be modelled with layer thicknesses as shown above (Figure 3.8 (a), $t_{\text{Ga}_2\text{O}_3} = t_{\text{ZrO}_2} = 60$ nm). The region between the two cut-off frequencies corresponds to green color. Green color ranges from 510 to 550 nm on the electromagnetic spectrum.

When the film thicknesses arranged as $t_{\text{Ga}_2\text{O}_3} = 130$ nm, $t_{\text{ZrO}_2} = 105$ nm, two notch filter behavior has been appeared. In the (b) part of Figure 3.8, one narrow and one relatively wide notch filter attitude is shown. Two centers of notch filter are located in the ultraviolet and infrared regions of the spectrum. Controlling the thickness also provides variety in terms of the number of notch filter centers.

Unlike previous works and examples, this simulation allows modeling various notch filters using more than two materials or different combinations.

Figure 5.14 (a) introduces a different periodic stack sort using two materials. Three film periods can be useful in some areas instead of pairs. In figure, SiO_2 - Y_2O_3 - SiO_2 films have been modeled on the top of each other with the their specific thicknesses;

$t_{SiO_2} = 70$ nm, $t_{Y_2O_3} = 70$ nm, $t_{SiO_2} = 90$ nm, respectively with $N = 15$. Filter attitude has been obtained between 790 and 945 nm on the spectrum.

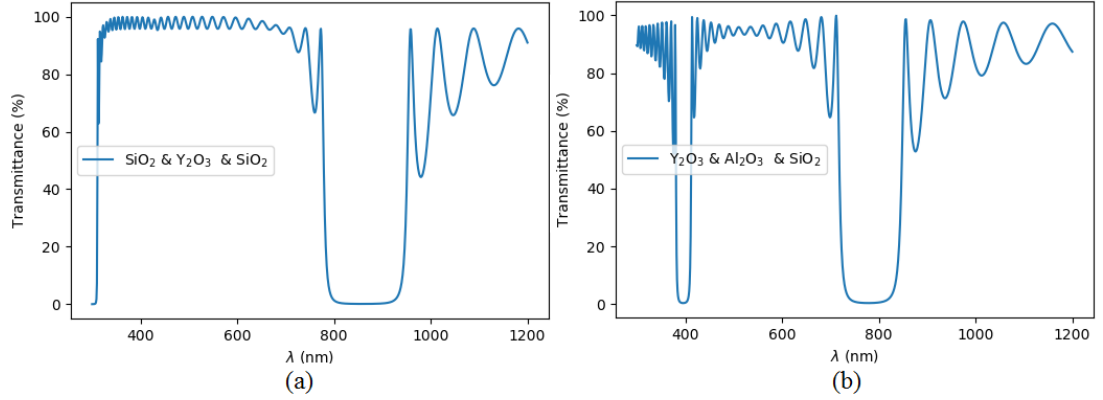


Figure 5.14 : Multilayer modeling of three materials combination.

This kind of large bandwidth filter is called stop-pass or minus filters. The bandwidth of the notch filter is 160 nm at FWHM. The example of three materials stack is given in figure 3.9 (b).

Two-centered notch filter behavior can be simulated using the Al₂O₃ - Y₂O₃ - SiO₂ thin film periods. The thickness of one period equals to $t_{Y_2O_3} = 70$ nm, $t_{Al_2O_3} = 70$ nm, $t_{SiO_2} = 90$ nm, respectively.

The number of periods is 20. The centers of the filter have corresponded to 400 and 780 nm. These two wavelengths belong to the boundaries of the visible region of the electromagnetic spectrum.

Fabrication

Afterward multilayer film stacks have been deposited using the E-beam system from low layer number and the layer number has been increased slightly. Transmittance and reflectance results of each deposited samples have been compared with simulation results.

As done in single-layer coatings, measured and simulated data have been plotted in the same graphs for each coating. After the simulation and experiment have been observed to be consistent for low layered structures, the number of periodic thin film layers (N) slightly increased in order to fabricate more dominant thin film notch filters.

Figures 5.15 – 5.18 show the transmission and reflection properties of the simulated and manufactured structures. Multilayer optical filters have been produced by

SiO₂-Al₂O₃ and Al₂O₃-Y₂O₃ thin film pairs with different film thicknesses and the number of film pairs.

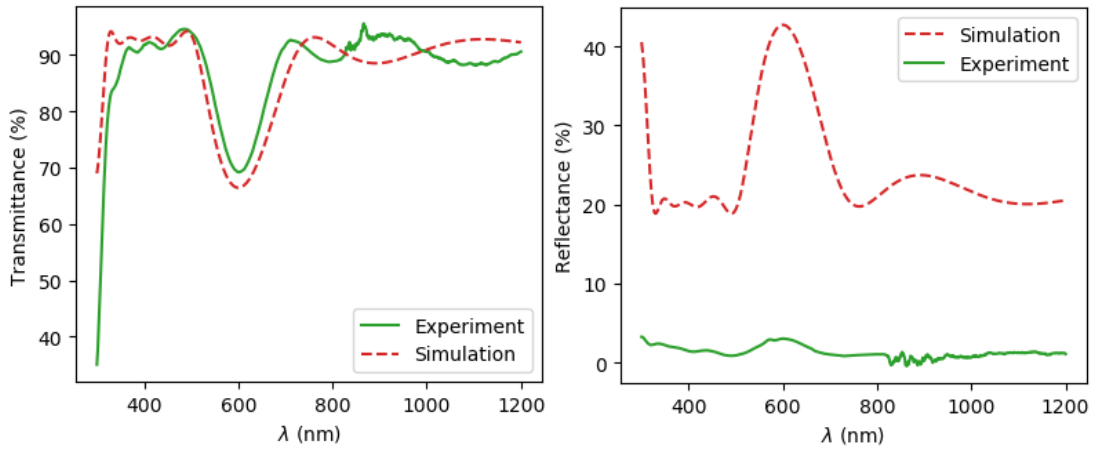


Figure 5.15 : Transmittance and reflectance of multilayer SiO₂(70nm) - Al₂O₃(110nm) coating, $N=4$.

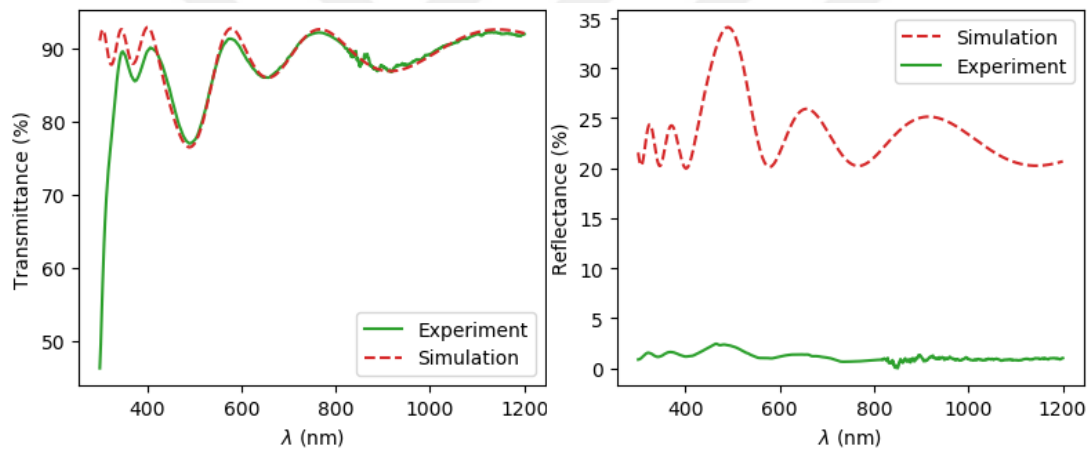


Figure 5.16 : Transmittance and reflectance of multilayer Al₂O₃(50nm) - Y₂O₃(75nm) coating, $N=5$.

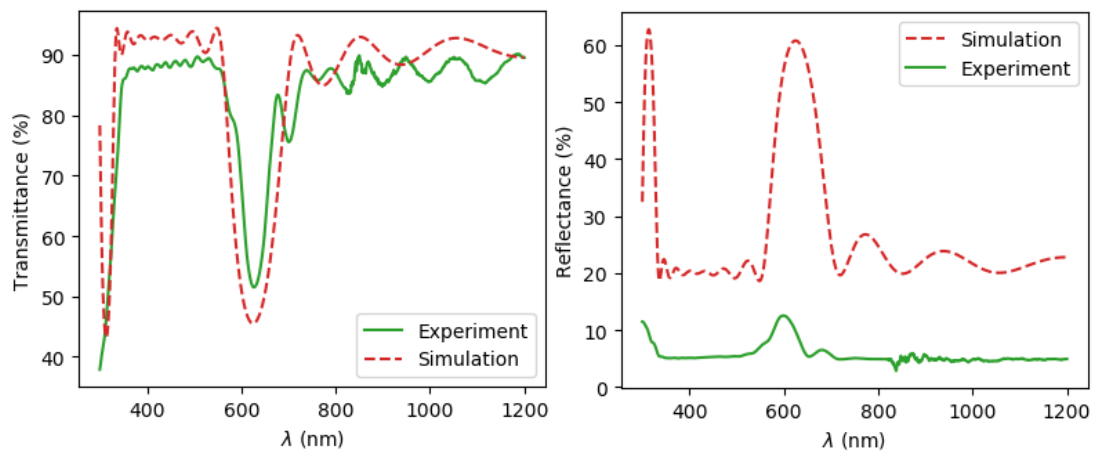


Figure 5.17 : Transmittance and reflectance of multilayer SiO₂(70nm) - Al₂O₃(110nm) coating, $N=7$.

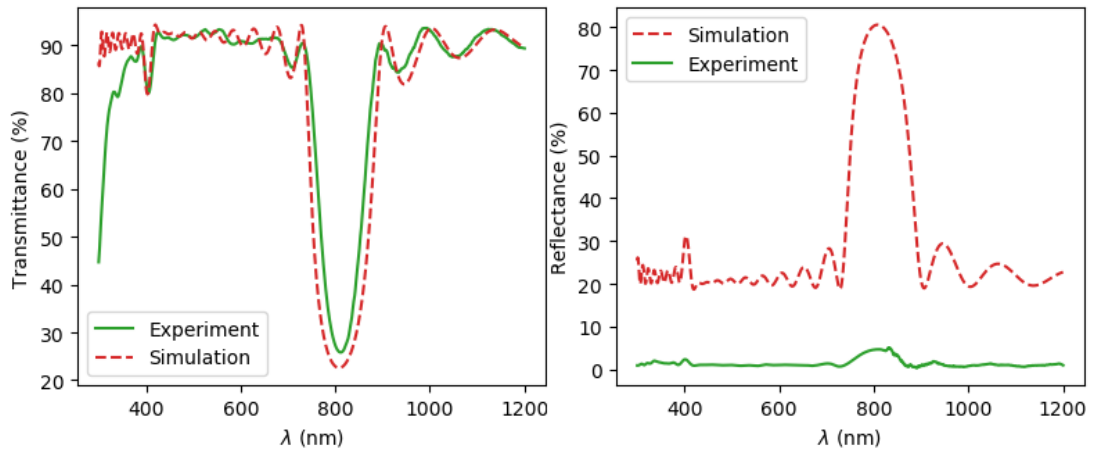


Figure 5.18 : Transmittance and reflectance of multilayer $\text{SiO}_2(130\text{nm})$ - $\text{Al}_2\text{O}_3(120\text{nm})$ coating, $N=10$.

It is seen in the figures above, as the number of pairs increases, the consistency of simulation has been maintained for all variables which are the type of film materials and their film thickness. The effect of thickness on the filtering location is seen.

Afterward, it has been decided to fabricate a thin film notch filter which consists of more film layers according to simulation outputs.

Figures 5.19 and 5.20 present the optical features of the produced thin film notch filters.

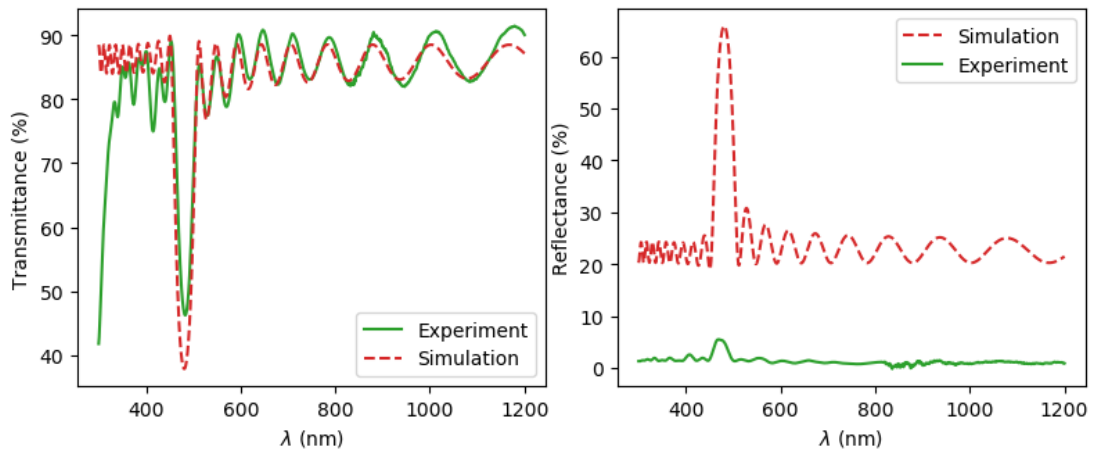


Figure 5.19 : Transmittance and reflectance of $\text{Al}_2\text{O}_3(50\text{nm})$ - $\text{Y}_2\text{O}_3(75\text{nm})$ thin film notch filter, $N=15$.

$\text{Al}_2\text{O}_3\text{-Y}_2\text{O}_3$ and $\text{SiO}_2\text{-Al}_2\text{O}_3$ filters exhibit notch filter attitude in the visible region of the electromagnetic spectrum, but they correspond to blue-green and orange colors, respectively. The number of film pair is 15 for both filters. It means filters have been made of 30 thin layers. The number of pairs has been restricted as 15 because of the limit of the coating system.

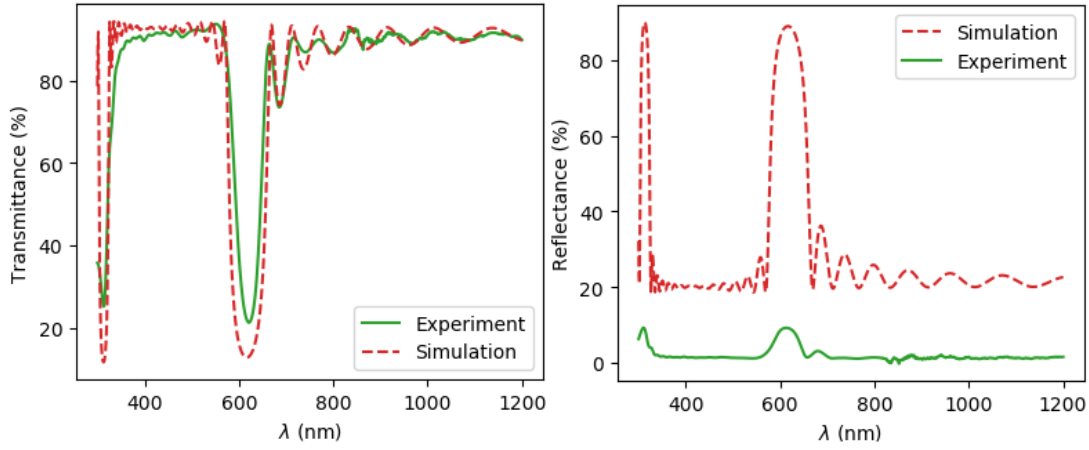


Figure 5.20 : Transmittance and reflectance of multilayer $\text{SiO}_2(70\text{nm})$ - $\text{Al}_2\text{O}_3(110\text{nm})$ thin film notch filter, $N=15$.

The mismatch in the reflectance of simulated and measured thin film notch filters is clearly seen in all figures. Moreover, when examining the transmittance and reflectance data of produced filters, it has been recognized that the sum of two data-set was not equal to 1. The reason for this inequality is the absorption of coatings.

Absorption has been neglected in the simulation calculations, so the incident light could be expressed as the sum of transmitted and reflected ratios of light. Optical characterizations of the fabricated thin film coatings have been shown that optical coatings absorb some ratio of the incoming electromagnetic wave. The absorption rate of produced thin film notch filters has been calculated according to Equation (2.45) and the results are shown in Figure 5.21.

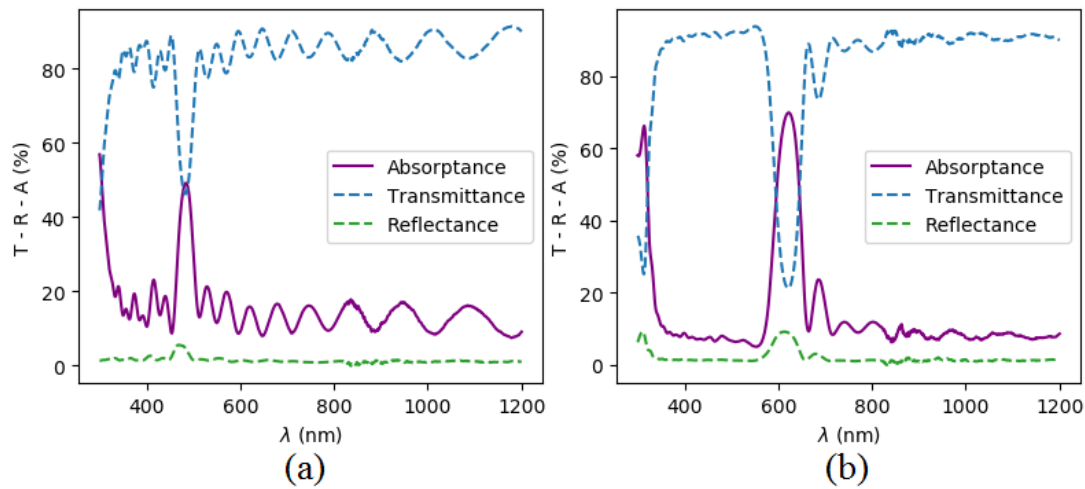


Figure 5.21 : Absorbance of produced thin film notch filters (a) $\text{Al}_2\text{O}_3(50\text{nm})$ - $\text{Y}_2\text{O}_3(75\text{nm})$, and (b) $\text{SiO}_2(70\text{nm})$ - $\text{Al}_2\text{O}_3(110\text{nm})$.

Figure 5.21 indicates that the filtering range between two cut-off frequencies is the more absorbed part. The absorption ratio in that part proportionally changes with the blocking intensity of the notch filter.

When Figure 5.14 (a) and Figure 5.14 (b) are compared, it can be said that the average absorptance ratio except filtering regions is approximately 10%. This rate can be associated with the substrate because both filters have been composed of different materials and total thickness, and the transmittance of the blank substrate was measured by approximately 91%.

5.4 Discussions

In the previous sections, the simulation has been proved its stability and usability for thin film notch filters. We decided to fabricate three thin film notch filters set about to work on different regions of the electromagnetic spectrum in the last part of the study.

All three-set filters have been fabricated with a 4.5 \AA/s deposition rate under a high vacuum condition. Center wavelengths (c_λ) of notch filters were determined as 480 nm, 620 nm, and 840 nm. Two of them have corresponding to the visible and other has been taken place in the near-infrared region of the electromagnetic spectrum. All filter sets have been produced with different layer numbers in order to observe the experimentally the effect of N . The wavelength-dependent transmittance graphics are presented in the following figures.

The produced thin film notch filter for the visible range of the electromagnetic spectrum is shown in Figure 5.15. The center wavelength is 480 nm and it corresponds to blue color in the visible band. The filter has been composed of Al_2O_3 and Y_2O_3 films. The thickness of each layer has been predicted by simulation for Al_2O_3 and Y_2O_3 thin films as 50 nm and 75 nm, respectively.

$N = 9$ and $N = 15$ samples have been well-matched with expectation, but the center wavelength of $N = 5$ sample has been shifted 10 nm right because of a 2 nm deviation of Y_2O_3 layers. According to simulation, film thicknesses of $N = 5$ coating are $t_{\text{Al}_2\text{O}_3} = 50 \text{ nm}$ and $t_{\text{Y}_2\text{O}_3} = 77 \text{ nm}$. So, it can be understood that 1 nm increasing in all film thickness causes a 5 nm deviation for the center wavelength of the notch filter.

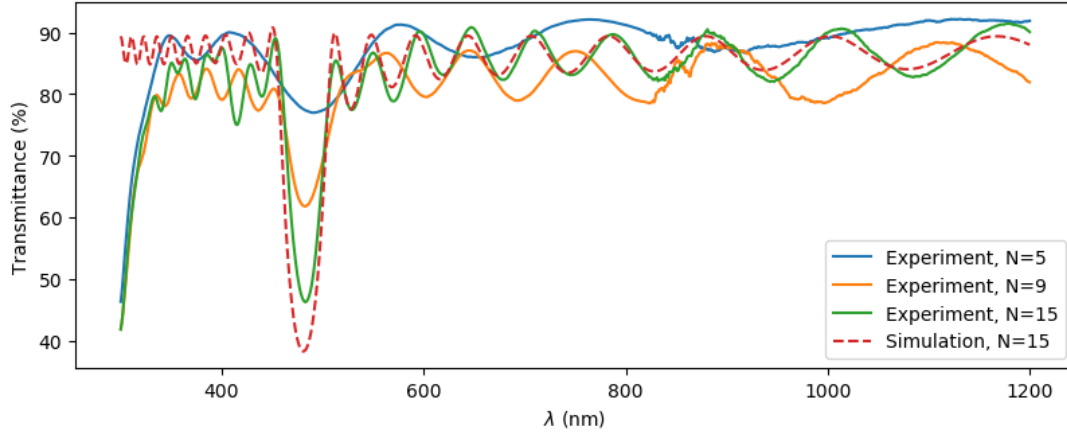


Figure 5.22 : Transmittance of fabricated $\text{Al}_2\text{O}_3\text{-Y}_2\text{O}_3$ thin film notch filter, $c_\lambda = 480$ nm

The second manufactured thin film notch filter has been also on the visible range. As distinct from, its center wavelength corresponds to orange color with 620 nm. The working range of the notch filter has been provided by $t_{\text{SiO}_2} = 70$ nm and $t_{\text{Al}_2\text{O}_3} = 110$ nm thin films.

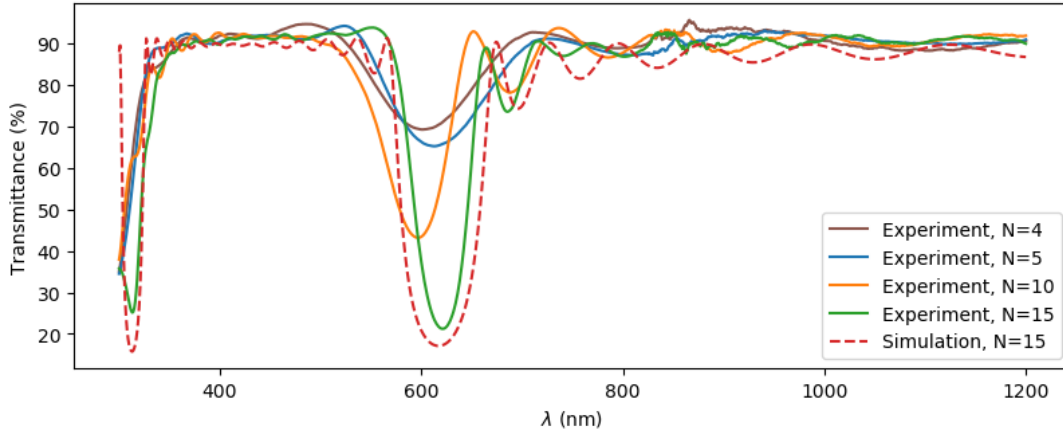


Figure 5.23 : Transmittance of fabricated $\text{SiO}_2\text{-Al}_2\text{O}_3$ thin film notch filter, $c_\lambda = 620$ nm.

Mismatchings on $N = 4$ and $N = 10$ samples have been standing out when Figure 5.16 was analyzed. Firstly, the simulation has been said that the coating thicknesses were 73 nm and 110 nm for SiO_2 and Al_2O_3 layers in $N = 4$ structure. +3 nm coating deviation in SiO_2 films dislocates the center wavelength of coating to 601 nm. Secondly, the center wavelength of $N = 10$ coating has been stated as 597 nm. The reason for the 23 nm sliding to left has arisen from the coating thickness of the Al_2O_3 thin films. The thickness of the Al_2O_3 layers has been detected as 65 nm. t_{SiO_2} is 110 nm for each layer of the $N = 10$ coating.

The last fabricated optical notch filter set by depositing SiO_2 and Al_2O_3 has corresponded to the near-infrared region of the spectrum which is shown in Figure 5.24. The center of the notch filter is equivalent the 840 nm.

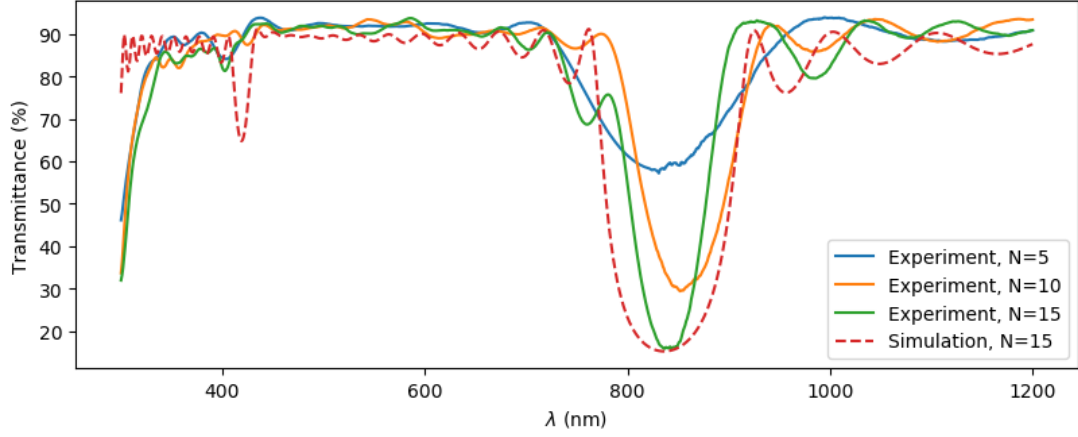


Figure 5.24 : Transmittance of fabricated $\text{SiO}_2\text{-Al}_2\text{O}_3$ thin film notch filter, $c_\lambda = 840$ nm.

The film thickness of SiO_2 and Al_2O_3 is the same and it is equal to 130 nm each in the multilayer stack. The filtering center of the $N = 10$ coating has been shifted to 845 nm due to its film thickness. $t_{\text{SiO}_2} = t_{\text{Al}_2\text{O}_3} = 131$ nm for $N = 10$ structure according to simulation. 1 nm increasing in all thin film layers has been influenced 5 nm the center wavelength of notch filter.

The specifications of the fabricated whole thin film notch filters with $N = 15$ are given in Table 5.9. Besides, application areas where they can be used will be mentioned in the conclusion chapter.

The number of periodic thin film groups has been limited as 15 in the thin film notch filter deposition procedure because of several systematic reasons. Manufacturing of 30-layered structure takes almost 10 hours using the present coating system. The total duration of the coating process can be separated approximately as 3 hours vacuuming, 6 hours deposition, and 1 hour post-deposition processes. Moreover, in the deposition process, substrate temperature reaches a high point due to the high electron emission current and kinetic energy of adatoms. The temperature level of the substrate is important during coating because as temperature increases, the diffusion ability of layer atoms increases. Inter-layer diffusion among deposited thin films is not desired. Since the coated structure must remain layer by layer for high-quality thin film notch filter performance.

Table 5.9 : Specifications of the produced thin film notch filters.

Specifications	Center wavelength of the notch filter		
	480 nm	620 nm	840 nm
Dimensions	37.5 mm × 25 mm × 1 mm	37.5 mm × 25 mm × 1 mm	37.5 mm × 25 mm × 1 mm
Substrate	Corning®-2947 glass	Corning®-2947 glass	Corning®-2947 glass
Film materials	Al ₂ O ₃ and Y ₂ O ₃	SiO ₂ and Al ₂ O ₃	SiO ₂ and Al ₂ O ₃
Number of periodic thin film groups	15	15	15
Total thin film number	30	30	30
Thickness of each thin film	$t_{Al_2O_3} = 50 \text{ nm} \ \& \ t_{Y_2O_3} = 75 \text{ nm}$	$t_{SiO_2} = 70 \ \& \ t_{Al_2O_3} = 110 \text{ nm}$	$t_{SiO_2} = 130 \ \& \ t_{Al_2O_3} = 130 \text{ nm}$
Total coating thickness	1875 nm	2700 nm	3900 nm
Angle of incidence	Normal	Normal	Normal
Minimum transmittance at c_λ	46.0041%	21.2833%	15.9848%
Cut-off wavelengths	457 nm - 508 nm	578 nm - 657 nm	771 nm - 902 nm
Filtering band width at FWHM	110 nm	220 nm	330 nm
Average transmittance (outside filtering band)	84.7512%	90.7055%	91.0012%
Average reflectance	1.2921%	2.0143%	1.7356%
Average absorptance	13.9567%	7.2803%	7.2524%

6. CONCLUSION

The demand for optical coatings has been increasing with developments in technologies in the last decades. Optical features of the surface can be modified by optical coatings. Multilayer thin film filters are a type of optical coating. Optical filters provide to increase or decrease optical ratios which are transmission, reflection, and absorption. Optical notch filters are the most complex ones among the thin film filter because of having two cut-off frequencies. And they work in a narrow range on the electromagnetic spectrum. The main purpose of this study is to model unique thin film notch filters by our software and to fabricate accurately them according to simulation results.

In this thesis, the thin film notch filter simulation has been created using Python and Jupyter Notebook according to the fundamentals of optical principles of thin films. Not only commonly used but also previously unused dielectric materials have been defined in the simulation as the material library with their Sellmeier dispersion equations. Optical basics and working principles of thin film notch filters have been explained in detail.

After numerical modeling of various thin film notch filters, thin film deposition methods have been examined and they have been explained. The E-beam evaporation method has been selected among PVD techniques for the fabrication of simulated thin film notch filters.

Al_2O_3 , Y_2O_3 , and SiO_2 have been chosen as film material and they were used in fabrication procedures. For achieving the same results with the simulation, thickness calibration and simulation correction have been done. In order to calibrate the coating system and adjust simulation, single-layer coatings have been simulated and produced. Using obtained transmission and thickness results from single-layer coatings, the calibration process has been completed. Moreover, the effects of deposition rate and film thickness on the surface roughness have been studied using single-layer coatings for each chosen material.

After reaching adequate consistency between the simulations and producing results, multilayer thin film notch filters have been fabricated. The effect of deposited layer number and thickness on the filter attitude has been investigated. Three types of thin film notch filters have been fabricated about to work on different regions of the electromagnetic spectrum. Their optical properties have been studied. Each produced notch filter can be used for different applications in various fields. The possible using areas of fabricated thin film notch filters have been surveyed.

The first produced thin film notch filter has been worked in the visible region. The center wavelength of the filter is 480 nm. This notch filter can be used in blocking monochromatic band applications. Also, after slight adjustment in the thickness of the layers, it can be used in Raman spectrometers which need notch filter that used for blocking laser beams (514 nm) inside the device in order to avoid noises during the measurement.

The second fabricated notch filter also can be used in monochromatic filtering applications. Both this filter ($c_\lambda = 620$ nm) and the latter filter ($c_\lambda = 480$ nm) can be an option for the treatment of migraine and photophobia. If some specific glasses are coated with thin films to decrease transmittance of visible lights (especially yellow and orange colors because the human eye is highly sensitive in this band), they may be a useful adjunct to reduce the harmful effects of migraine and photophobia.

The third fabricated multilayer thin film notch filter, has been worked in the near-infrared region of the spectrum. So, this filter can be used in specific spectrometers and sensors which work in the near-infrared region of the electromagnetic spectrum.

In summary, numerous thin film notch filters and single-layer coatings have been designed through the simulation during the present study. 8 single-layer coatings have been produced using selected dielectric materials for calibration, correction, and analysis. Besides, numerous multilayer thin film notch filters have been simulated using not only commonly used but also unused material combinations with periodic two or three thin film stack. Some of them, SiO_2 -h-BN, Al_2O_3 - Y_2O_3 , Ga_2O_3 - ZrO_2 , SiO_2 - Y_2O_3 - SiO_2 , and Y_2O_3 - Al_2O_3 - SiO_2 , have been presented. Three-set multilayer

thin film notch filters from 8-layer to 30-layer have been fabricated using the E-beam evaporation technique after designing by the simulation for various applications.

As future work, the simulation can be improved in two ways. First is combining present simulation with various algorithms. Thus, more sensitive thin film notch filters and unimaginable variations can be simulated. Second, the simulation can be enhanced in order to model the optical behaviors of metamaterials; thereby it is possible to design structures that have a negative refractive index.





REFERENCES

- [1] **Young, T.** (1804). The Bakerian Lecture: Experiments and Calculations Relative to Physical Optics, *Philosophical Transactions of the Royal Society of London Series I*, 94, 1–16.
- [2] **Barutçu, B.**, (2012), The design and production of interference edge filters with plasma ion assisted deposition technique for a space camera, *M.Sc. thesis*, Middle East Technical University, Ankara, Turkey.
- [3] **Knittl, Z.** (1976). *Optics of Thin Films*, Wiley & Sons, Czechoslovakia, 1. edition.
- [4] **Aydın, E.**, (2011), Notch filter design, *M.Sc. thesis*, Ankara University, Ankara, Turkey.
- [5] **Rayan, D., Elbashar, Y., Rashad, M. and El-Korashy, A.** (2013). Optical spectroscopic analysis of cupric oxide doped barium phosphate glass for bandpass absorption filter, *Journal of Non-Crystalline Solids*, 382, 52–56.
- [6] **Vukusic, P.** (2003). *Optical Interference Coatings*, Springer, Berlin, Heidelberg, Innsbruck, Austria, 1. edition.
- [7] Newport Thin Film Laboratory, <http://www.newportlab.com>, last accessed date: 02.01.2020.
- [8] **Verhoeven, G.** (2017). The reflection of two fields – electromagnetic radiation and its role in (aerial) imaging, *AARGnews*, 55, 13–18.
- [9] **Correia, J.H., Emadi, A.R. and Wolffenbuttel, R.F.** (2007). UV bandpass optical filter for microspectrometers, *ECS Transactions*, 141–147.
- [10] **Macleod, H.A.** (2001). *Thin Film Optical Filter*, McGraw-Hill, New York, USA.
- [11] **Hoggan, R.N., Subhash, A., Blair, S., Digre, K.B., Baggaley, S.K., Gordon, J. and Katz, B.J.** (2016). Thin-film optical notch filter spectacle coatings for the treatment of migraine and photophobia, *Journal of Clinical Neuroscience*, 28, 71–76.
- [12] **Griffiths, D.J.** (1999). *Introduction to Electrodynamics*, Prentice Hall International Limited, London, UK, 3. edition.
- [13] **Pedrotti, F.L. and Pedrotti, L.S.** (1993). *Introduction to Optics*, Prentice Hall International Limited, London, UK, 2. edition.
- [14] **Ohring, M.** (1992). *The Materials Science of Thin Films*, Academic Press, New Jersey, USA, 1. edition.

- [15] **Gaillet, M. and Pervychine, N.** (2006). Cauchy and related empirical dispersion formulae for transparent materials, *HORIBA Jobin Yvon - Technical Note-TN14*.
- [16] **Liu, Y. and Daum, P.H.** (2008). Relationship of refractive index to mass density and self-consistency of mixing rules for multicomponent mixtures like ambient aerosols, *Journal of Aerosol Science*, 39(11), 974 – 986.
- [17] **Devore, J.R.** (1951). Refractive indices of rutile and sphalerite, *J. Opt. Soc. Am*, 41, 416 – 419.
- [18] **Malitson, I.H.** (1965). Interspecimen comparison of the refractive index of fused silica, *J. Opt. Soc. Am*, 55, 1205 – 1208.
- [19] **Bodurov, I., Vlaeva, I., Viraneva, A., Yovcheva, T. and Sainov, S.** (2016). Modified design of a laser refractometer, *Nanoscience & Nanotechnology*, 16, 31 – 33.
- [20] **Bhaumik, I., Bhatt, R., Ganesamoorthy, S., Saxena, A., Karnal, A.K., Gupta, P.K., Sinha, A.K. and Deb, S.K.** (2011). Temperature-dependent index of refraction of monoclinic Ga₂O₃ single crystal, *Optical Society of America*, 50(31), 6006 – 6010.
- [21] **Nigara, Y.** (1968). Measurement of the optical constants of yttrium oxide, *Jpn. J. Appl. Phys*, 7, 404 – 408.
- [22] **Malitson, I.H. and Dodge, M.J.** (1972). Refractive index and birefringence of synthetic sapphire, *J. Opt. Soc. Am*, 62, 1405.
- [23] **Pastrňák, J. and Roskocová, L.** (1966). Refraction index measurements on AlN single crystals, *Phys. Stat. Sol*, 16, K5 – K8.
- [24] **Lee, S.Y., Jeong, T.Y., Jung, S. and Yee, K.J.** (2018). Refractive index dispersion of hexagonal boron nitride in the visible and near-infrared, *Physica Status Solidi (b)*, 256, 1800417.
- [25] Refractive Index Database, <https://refractiveindex.info>, last accessed date: 22.01.2020.
- [26] **Kashin, A. and Ananikov, V.** (2011). A SEM study of nanosized metal films and metal nanoparticles obtained by magnetron sputtering, *Russ. Chem. Bull.*, 60, 2602–2607.
- [27] Farotex LLP, <http://https://farotex.com/technology.html>, last accessed date: 15.02.2020.
- [28] **Lei, K.F.** (2015). Materials and fabrication techniques for nano- and microfluidic devices, *Microfluidics in Detection Science: Lab-on-a-chip Technologies*, 1–28.
- [29] **Oleiwi, H.F., Al-Taay, H.F., Al-Ani, S.K.Y. and Tahir, K.J.** (2019). Structural and optical properties of Al₂O₃ nanocrystalline: Effect of deposition time, *AIP Conference Proceedings*, 2144(1), 030027.

- [30] **Zhidkov, I.S., Kukharenko, A.I., Maksimov, R.N., Finkelstein, L.D., Cholakh, S.O., Osipov, V.V. and Kurmaev, E.Z.** (2019). Optical transparency and local electronic structure of Yb-doped Y2O3 ceramics with tetravalent additives, *Symmetry*, *11*(2).
- [31] **Friz, M. and Waibel, F.** *Coating Materials*, [online], <http://www.tsvacuum.com/spanish/UploadFiles/200813112542318.pdf>.
- [32] **Leng, D., Wu, L., Hongchao, J., Zhao, Y., Li, W. and Feng, L.** (2012). Preparation and properties of SnO2 film deposited by magnetron sputtering, *International Journal of Photoenergy*, 2012.
- [33] **Stampfer, C., Jungen, A. and Hierold, C.** (2006). Fabrication of discrete nanoscaled force sensors based on single-walled carbon nanotubes, *Sensors Journal, IEEE*, *6*, 613 – 617.



APPENDICES

APPENDIX A.1 : Materials Library

APPENDIX A.2 : Single-layer Modeling Function

APPENDIX A.3 : Multilayer Modeling Function





APPENDIX A.1

```
1 # -*- coding: utf-8 -*-
2 """
3 @author: Eray Humali
4 """
5
6 import numpy as np
7 import matplotlib.pyplot as plt
8 %matplotlib inline
9
10 eps0 = 8.85418782 * 1e-12 #permittivity of free space
11 mu0 = 4 * np.pi * 1e-7 #permeability of free space
12 n0 = 1 #refractive index of air
13 lamb = np.arange(300,1201,1)
14
15 #refractive index of some materials
16 n = {'Corning': np.sqrt(1 + 1.03961212*lamb**2/(lamb**2-6000.69867) +
17     0.231792344*lamb**2/(lamb**2-20017.9144) + 1.01046945*lamb**2/(lamb
18     **2-103560653))
19     , 'BK7': 1.5081 + lamb**2*0
20     , 'SiO2': np.sqrt(1 + (0.6961663*lamb**2/(lamb**2-68.4043**2)) +
21     (0.4079426*lamb**2/(lamb**2-116.2414**2)) + (0.8974794*lamb**2/(lamb
22     **2-9896.161**2)))
23     , 'TiO2': np.sqrt(5.913 + 0.2441*1e6/(lamb**2-0.0803*1e6))
24     , 'AlN': np.sqrt(1 + 2.1399 + 1.3786*lamb**2/(lamb**2-171.5**2) + 3.861*
25     lamb**2/(lamb**2-15030**2))
26     , 'Y2O3': np.sqrt(1 + 2.578*lamb**2/(lamb**2-138.71**2) + 3.935*lamb**2/(
27     lamb**2-22936**2))
28     , 'Al2O3': np.sqrt(1 + 1.4313493*lamb**2/(lamb**2-72.6631**2) + 0.65054713*
29     lamb**2/(lamb**2-119.3242**2) + 5.3414021*lamb**2/(lamb**2-18028.251**2))
30     , 'ZrO2': np.sqrt(1 + 3.3037*lamb**2/(lamb**2-198.7971**2))
31     , 'Ga2O3': np.sqrt(3.52594 + 0.04131*1e6/(lamb**2-0.03002*1e6 + lamb
32     *0.00885))
33     , 'h-BN': np.sqrt(1 + 3.263*lamb**2/(lamb**2-164.4**2))}
```

APPENDIX A.2

```
1 # -*- coding: utf-8 -*-
2 """
3 @author: Eray Humali
4 """
5
6 #single-layer transmittance & reflectance calculation
7 def TR(lamb, n0, n1, ns, t):
8
9     gamma_0 = n0 * np.sqrt(eps0 * mu0)
10    gamma_1 = n1 * np.sqrt(eps0 * mu0)
11    gamma_s = ns * np.sqrt(eps0 * mu0)
12
13    delta = 2*np.pi/lamb * n1 * t * np.cos(60)
14
15    M = np.array([[np.cos(delta), 1j * np.sin(delta) / gamma_1]
16                  , [1j * gamma_1 * np.sin(delta), np.cos(delta)]])
17
18    M11 = M[0,0]
19    M12 = M[0,1]
20    M21 = M[1,0]
21    M22 = M[1,1]
22
23    tr = 2*gamma_0 / (gamma_0*M11 + gamma_0*gamma_s*M12 + M21 + gamma_s*M22)
24    rf = (gamma_0*M11 + gamma_0*gamma_s*M12 - M21 - gamma_s*M22) / (gamma_0*
25    M11 + gamma_0*gamma_s*M12 + M21 + gamma_s*M22)
26
27    T = (ns/n0) * abs(tr)**2 * 100
28    R = 100 - T
29
30    return T, R
31
32 T_Al2O3 = []
33 R_Al2O3 = []
34 for i in range(len(lamb)):
35     t, r = TR(lamb[i], n0, n['Al2O3'][i], n['Corning'][i], 125)
36     T_Al2O3.append(t)
37     R_Al2O3.append(r)
38 T_Al2O3 = np.array(T_Al2O3)
39 R_Al2O3 = np.array(R_Al2O3)
40
41 T_Y2O3 = []
42 R_Y2O3 = []
43 for i in range(len(lamb)):
44     t, r = TR(lamb[i], n0, n['Y2O3'][i], n['Corning'][i], 118)
45     T_Y2O3.append(t)
46     R_Y2O3.append(r)
47 T_Y2O3 = np.array(T_Y2O3)
48 R_Y2O3 = np.array(R_Y2O3)
49
50 T_SiO2 = []
51 R_SiO2 = []
52 for i in range(len(lamb)):
53     t, r = TR(lamb[i], n0, n['SiO2'][i], n['Corning'][i], 120)
54     T_SiO2.append(t)
55     R_SiO2.append(r)
56 T_SiO2 = np.array(T_SiO2)
57 R_SiO2 = np.array(R_SiO2)
```

APPENDIX A.3

```

1  #-*- coding: utf-8 -*-
2  """
3  @author: Eray Humali
4  """
5
6  #multilayer transmittance & reflectance calculation
7  def multi(lamb, n0, ns, nL, nH, tL, tH, N):
8
9      gamma_0 = n0 * np.sqrt(eps0 * mu0)
10     gamma_s = ns * np.sqrt(eps0 * mu0)
11     gamma_L = nL * np.sqrt(eps0 * mu0)
12     gamma_H = nH * np.sqrt(eps0 * mu0)
13
14     delta_L = 2*np.pi/lamb * nL * tL * np.cos(60)
15     delta_H = 2*np.pi/lamb * nH * tH * np.cos(60)
16
17     ML = np.array([[np.cos(delta_L), 1j * np.sin(delta_L) / gamma_L],
18                   [1j * gamma_L * np.sin(delta_L), np.cos(delta_L)]])
19
20     MH = np.array([[np.cos(delta_H), 1j * np.sin(delta_H) / gamma_H],
21                   [1j * gamma_H * np.sin(delta_H), np.cos(delta_H)]])
22
23     M = np.linalg.matrix_power(MH.dot(ML), N)
24
25     M11 = M[0,0]
26     M12 = M[0,1]
27     M21 = M[1,0]
28     M22 = M[1,1]
29     beta = ns/n0
30
31     tr = 2*gamma_0 / (gamma_0*M11 + gamma_0*gamma_s*M12 + M21 + gamma_s*M22)
32
33     T = beta * abs(tr)**2 * 100
34     R = (1 - T) * 100
35
36     return T, R
37
38 T_1 = []
39 R_1 = []
40 for i in range(len(lamb)):
41     tr, rf = multi(lamb[i], n0, n['Corning'][i], n['Al2O3'][i], n['SiO2'][i],
42                   70, 110, 5)
43     T_1.append(tr)
44     R_1.append(rf)
45 T_1p = np.array(T_1)
46 R_1p = np.array(R_1);
47
48 T_2 = []
49 R_2 = []
50 for i in range(len(lamb)):
51     tr, rf = multi(lamb[i], n0, n['Corning'][i], n['Al2O3'][i], n['SiO2'][i],
52                   70, 110, 10)
53     T_2.append(tr)
54     R_2.append(rf)
55 T_2p = np.array(T_2)
56 R_2p = np.array(R_2);
57
58 T_3 = []
59 R_3 = []
60 for i in range(len(lamb)):
61     tr, rf = multi(lamb[i], n0, n['Corning'][i], n['Al2O3'][i], n['SiO2'][i],
62                   70, 110, 15)
63     T_3.append(tr)
64     R_3.append(rf)
65 T_3p = np.array(T_3)
66 R_3p = np.array(R_3);

```



CURRICULUM VITAE

Name Surname: Eray HUMALI

Place and Date of Birth: Uşak / 27.04.1994

E-Mail: erayhumali@gmail.com



EDUCATION:

- **M.Sc.:** 2020, Istanbul Technical University, Department of Materials Engineering
- **B.Sc.:** 2018, Istanbul Technical University, Department of Physics Engineering (Major)
- **B.Sc.:** 2018, Istanbul Technical University, Department of Chemistry (Minor)
- **B.Sc.:** 2016, Umeå University, Department of Physics Engineering (Erasmus+)

PROFESSIONAL EXPERIENCE:

- 2020-ongoing, R&D Engineer, ROKETSAN Missiles Inc., BLS–Missile and Artillery Systems Center
- 2018-2019, Researcher, Istanbul Technical University, TÜBİTAK–1003 Project
- 2017, Intern, ASELSAN Inc., ASELSAN Research Center
- 2016, Intern, ACIBADEM Healthcare Group, Department of Radiation Oncology

PUBLICATIONS, PRESENTATIONS AND PATENTS:

- Karaağaç, H., Güller, Ö., Peksu, E., Humalı, E., Termezoğlu, M., Parlak, M., 2019. Transfer of ordered and disordered Si nanowires onto alien substrates for the fabrication of third-generation solar cells., *Proc. SPIE 10982, Micro- and Nanotechnology Sensors, Systems, and Applications XI*, 1098205, DOI:10.1117/12.2518610.
- Humalı E., Peksu E., Karaağaç, H., 2019. Fabrication and Characterization of n-Si-Nanowires/p-CZTS structured Solar Cells on Transparent Conducting Oxides Substrates. *European Materials Research Society (E-MRS) 2019 Meeting*, May 28-30,2019 Nice, France.
- Humalı E., Alveroğlu E., 2018. Synthesis & Characterization of Cu Doped Fe₃O₄ Magnetic Nanoparticles. *14th Nanoscience and Nanotechnology Conference of Turkey (NANOTR)*, September 22-25,2018 İzmir, Turkey.

- Humalı, E., G ng r G., ITUNOVA TTT, 2017. Radyoterapi Lineer Hızlandırıcılarında Vol metrik Ark Terapi (VMAT) Teknięi ile Kullanılabilecek Kan Işınlama Fantomu. Patent Number: 2017-GE-289681 (Status: Pending)
- G ng r, G., Humalı, E. A Simple VMAT Method for Blood Irradiation Procedure, - *Work in progress*,

